

Transition of AC electroosmotic flow from linear to nonlinear state in different pH environment

Yu Han^{1,#}, Zhongyan Hu^{1,#}, Kaige Wang¹ and Wei Zhao^{1,*}

¹ State Key Laboratory of Photon-Technology in Western China Energy, International Scientific and Technological Cooperation Base of Photoelectric Technology and Functional Materials and Application, Laboratory of Optoelectronic Technology of Shaanxi Province, Institute of Photonics and Photon-Technology, Northwest University, Xi'an, 710127, China

The authors contributed equally to this investigation

* Correspondence: zwbayern@nwu.edu.cn

Abstract: Electroosmotic flow (EOF) exists widely at the solid-liquid interface in the presence of external electric field. However, the EOF driven by an alternating current (AC) electric field in diverse chemical environments was far from being well understood due to limited experimental investigations. In this investigation, through the high-resolution laser-induced fluorescent photobleaching anemometer (LIFPA), the transient velocity according to the AC EOF on the electric double layer (EDL) far from the electrodes has been experimentally characterized, by means of time series and power spectra. With analyzing the transient velocity, the transition of AC EOF from linear to nonlinear behavior is observed in a broad parameter space, e.g. mean flow velocity, the frequency and intensity of the AC electric field, and the pH value of the bulk fluid. To take all these parameters into account, an electro-inertial velocity has been applied as the characteristic velocity, instead of the commonly applied Helmholtz-Smoluchowski velocity. Then, the transitional electric field intensity $E_{A,C}$ and the corresponding dimensionless parameter Z_{nlc} are systematically studied. A power-law relationship between the linear term coefficient Z_l and Z_{nlc} has been established, with the scaling exponents determined by the pH value of the electrolyte solution. We hope the current investigation can provide a deeper understanding of the transition of AC EOF and the instantaneous response of EOFs in other forms. It also provides a simple model to understand the coupling between electric field and fluid flow, in both linear and nonlinear status.

1. Introduction

In the past two decades, electroosmotic flows (EOFs) driven by temporally varied alternating current (AC) electric fields, e.g. periodic or modulated electric fields, are commonly applied or existed in engineering applications, e.g. biomedicine, micro/nanofluidics, electrochemistry system and energy industry, etc. In the biomedical field, AC EOF have been developed rapidly and widely applied for manipulating biological and biomedical targets, such as DNA biosensor (Wu *et al.* 2015), DNA concentrators (Bown & Meinhart 2006; Lei *et al.* 2009; Wong *et al.* 2004), DNA hybridization (Das & Chakraborty 2007), DNA electrophoresis (Khodabandehloo & Chen 2017), bacteria detection (Gagnon & Chang 2005) and virus infection diagnosis (Arima *et al.* 2021). In micro/nanofluidics, AC EOF widely exists in the transportation and manipulation of fluids (Sphaier 2012; Wu & Chen 2019; Yu *et al.* 2023), samples (Bera & Bhattacharyya 2013; Das *et al.* 2007; Liu *et al.* 2020; Wu *et al.* 2022) and ionic circuits (Leong *et al.* 2020). In the electrochemistry field, AC EOF is also broadly applied for electrochemical analysis (Wang *et al.* 2009), electrodeposition (Han *et al.* 2016; Ji *et al.* 2014), and soil treatment (Martin *et al.* 2019; Probstein & Hicks 1993). In the energy industry, AC EOF is closely associated with energy production and storage, such as the charging-discharging cycles of supercapacitors (Agar *et al.* 2013; Feng & Cummings 2011) and liquid electrolyte batteries

(Romanyuk *et al.* 2016; Wang *et al.* 2020), both adjacent to electrodes (Bhattacharyya & Gopmandal 2013) and the far away counterparts (Yang *et al.* 2015), if fast charge-discharge is required.

The simplest electrokinetic (EK) flow model has been diagrammed in Figure 1, where two electrodes and one long straight channel with insulated walls are present. Two types of electric structures, i.e. the commonly termed electric double layer (EDL) or electric triple layer (ETL), are formed on the surfaces of insulating walls and electrodes respectively.

When an AC electric field with low amplitude is applied on the electrodes, the EDLs on electrode surfaces maintain equilibrium status. The internal electric field on bulk fluids responds linearly to the external AC electric field, and accordingly, an oscillating EOF (OEOF) can be generated on the insulated bottom walls, oscillating linearly with the external AC electric field. This type of linear AC EOF has been comprehensively investigated numerically and experimentally for both Newtonian (Chakraborty & Srivastava 2007; Dutta & Beskok 2001; Kneller *et al.* 2016; Ramos *et al.* 2005; Zhao *et al.* 2018) and non-Newtonian fluids (Jian *et al.* 2011). Dutta and Beskok (2001) theoretically studied the velocity fluctuations of the AC EOF in a parallel plate microchannel under the approximation of thin EDL and made preliminary predictions on the influence of electric field intensity and frequency. At the same time, they found that there was an inflection point in the vertical velocity fluctuation profile, and the flow might be unstable. Ramos *et al.* (2005) used a linear EOF model based on the Debye-Huckel theory to analyze the influence of voltage on velocity fluctuations. At low voltages, the voltage-velocity relationship follows a linear curve that is consistent with the theoretically predicted linear model. While at high voltages, the direction of flow can vary with the applied AC voltage, creating a countercurrent that affects the motion of the fluid. When the frequency exceeds a certain limit, the linear model has a large deviation from experimental results and a more comprehensive model is required to explain this phenomenon.

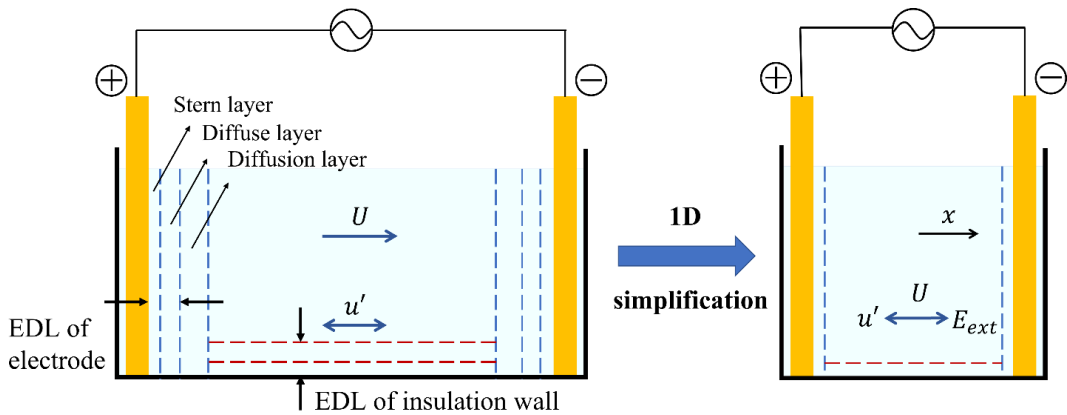


Figure 1 Schematic and the 1D approximation of the AC EOF model.

In recent years, with the rapid development of batteries, electrochemistry, and other fields, nonlinear AC EOF generated by high voltage and strong electric fields become important. When the electric field is sufficiently high, nonlinear electric field on the electrodes surface caused by ion concentration polarization (ICP) can be generated and results in a series of nonlinear flow phenomena. For instance, Rubinstein and Zaltzman (2000; 2007) predicted that when the external voltage applied to the ion-selective membrane was greater than the critical voltage, vortical flow can be induced by the so-called Rubinstein-Zaltzman instability around electrodes. Bazant *et al.* (2004) studied the weak and strong nonlinear phenomena in the triple-layer structures (Stern-Diffuse-Diffusion layer) of electrodes under a DC electric field by numerical simulation. In the weakly nonlinear regime, the fluctuation of the ion concentration in the diffusion layer is negligible compared to the bulk value, while in the strongly nonlinear regime, a sharp fluctuation of the ion concentration can be present in the diffusion layer. Later, Olesen *et al.* (2010) studied the dynamics of weakly and strongly nonlinear EOF on the electrode surface under AC voltages. As the voltage

increases, the weakly nonlinear electrostatics will be destroyed. In turn, the strongly nonlinear regime becomes important, characterized by local salt depletion in the diffusion layer near the electrodes and the breakdown of the quasi-equilibrium structure of the double layers. Both the weakly and strongly nonlinear electric field in EDL of electrodes can cause a nonlinear response of the electric field in the bulk fluids, and subsequently, induce nonlinear EOF on the insulated walls. Schnitzer and Yariv (2014) theoretically analyzed the nonlinear AC EOF under the approximation of thin EDL and advanced an approximate analytical solution of the electric potential based on a simplified dynamic model. Stout and Khair (2015) quantified the diffusion charge dynamics of a symmetric binary electrolyte at moderately nonlinear AC voltages, which exhibit a symmetric deviation from the (uniform) equilibrium density at even-order voltage amplitudes.

At present, the researches on the intrinsic dynamics of AC EOF mainly rely on numerical and theoretical methods. Experimental investigations on the instantaneous flow dynamics of AC EOF are relatively limited and primarily in an indirect manner. For instance, Santiago et al. (1998) studied the average velocity of AC EOF using a micro-particle image velocimetry (μ PIV) system with a Reynolds number of 3×10^{-4} . Wu et al. (2013) used μ PIV to experimentally study low-frequency AC EOF by phase averaging. However, due to the limited spatial resolution of μ PIV, they are unable to accurately measure fluid velocity fluctuations on or adjacent to EDL. At the same time, μ PIV uses fluorescent particles as series particles to characterize the velocity field, while the hysteresis effect of the particles makes it difficult to measure high-frequency and strong velocity fluctuations. Although some experimental investigations (Rubinstein *et al.* 2008; Suh & Kang 2008; Suh & Kang 2009; Yossifon & Chang 2008) have revealed the flow feature of EOF primarily in strongly nonlinear regime, the understanding of the transition of AC EOF is still far from sufficient.

Recently, with laser-induced fluorescent photobleaching anemometer (LIFPA) (Wang 2005) technique, Zhao et al. successfully measured the instantaneous velocity fluctuations of both linear (Zhao *et al.* 2018) and nonlinear AC EOFs (Hu *et al.* 2020; Hu *et al.* 2021; Hu *et al.* 2022) at the positions adjacent to the EDL of insulated wall. They revealed, in linear AC EOF, when the frequency (f_f) of AC electric field gradually increases, the mean square value of the velocity fluctuation— u_{rms} decreases as $f_f^{-0.66}$. This result is different from the predictions of the previous theory, e.g. (Dutta & Beskok 2001), and implies the response of AC EOF to external AC electric field is slower than theoretical prediction. Their further investigations on the velocity fluctuations of nonlinear AC EOF reveal there could be a different status of nonlinear AC EOF, if the applied basic flow rate, frequency, and intensity of AC electric field are different. The AC EOF can be either periodic, quasiperiodic, or chaotic. (Hu *et al.* 2021) In 2022, Hu et al. carried out a detailed experimental investigation on the transition of AC EOF from linear to nonlinear regime. (Hu *et al.* 2022) They showed the transition electric field can be accurately measured through the emergence of 2nd harmonic frequency in the power spectra of velocity fluctuations. Their investigations further revealed that the dimensionless control parameters, i.e. Z_l (determines the linear behavior) and Z_{nlc} (determines when the nonlinear behavior becomes non-negligible), had shown a power-law relationship. Nevertheless, in the investigation, the flow velocity is characterized by Helmholtz-Smoluchowski velocity (which is intrinsically an electroviscous velocity), which cannot elucidate the influence of pH value on the status of AC EOF.

The purpose of this paper is to conduct a detailed and systematic experimental study on the transition of AC EOF from linear to weakly nonlinear status, concerning the influence of pH value. The paper is organized as follows. In section 2, the setup and procedures of LIFPA measurement are introduced. Then, in section 3, the one-dimensional (1D) approximation of AC EOF model has been analyzed. Instead of the commonly used Helmholtz-Smoluchowski velocity, an electro-inertial velocity has been adopted as the characteristic velocity in dimensionless parameters. In section 4, the experimental results are further analyzed according to the dimensionless parameters. Here, the important physical and chemical control parameters, e.g. basic flow velocity, frequency and intensity of AC electric field, pH value of solution, etc., have all been taken into account. The critical curves that divide the linear and weakly

nonlinear regimes of AC EOF have been obtained. At last, the universality of dimensionless parameters and the governing equations on AC EOF is discussed.

2. Experimental setup

2.1 LIFPA system developed on a confocal microscope

LIFPA is a novel micro/nanofluidics velocity measurement technique based on laser induced fluorescence (LIF) and photobleaching effect. It was first proposed and developed by Wang in 2005. (Wang 2005) This method measures microflow velocity based on the relationship between convection velocity of fluorescent solution and fluorescent intensity with the presence of photobleaching. LIFPA has ultrahigh spatial and temporal resolutions with electric neutrality which make LIFPA compatible for studying transient EK flow. For instance, Wang, Zhao, and their collaborators have used LIFPA to characterize EK turbulent flow (Wang *et al.* 2016; Wang *et al.* 2014; Zhao *et al.* 2021; Zhao *et al.* 2017) in a micromixer, and linear/nonlinear EOF on the insulated wall (Hu *et al.* 2020; Hu *et al.* 2021; Hu *et al.* 2022; Zhao *et al.* 2018). In these investigations, LIFPA can measure velocity fluctuations up to 3 kHz with a spatial resolution of ~ 200 nm. (Zhao *et al.* 2018)

The LIFPA system in this investigation is diagramed in Figure 2(a). It is developed based on a confocal microscopy system, which contains a 405 nm continuous wave laser (MDL-III-405-500), $100\times$ NA1.4 PlanApo oil immersion objective lens (Olympus), dichroic mirror (Semrock, FF506-Di03) and other optical elements. The dichroic mirror has a reflection band around 405 and 532 nm, and a transmission band of 420-520 nm. The fluorescent signal after excitation passes through the objective lens and the dichroic mirror in sequence, is then collected by a multimode optical fiber (Thorlabs, diameter 25 μm , 400-550 nm band) after a bandpass filter set (combined by a wideband filter 470/100 nm and a narrowband filter 470/10 nm). The fluorescent signal is finally measured by an APD photomultiplier tube (PMT, Hamamatsu H7421). Since the APD PMT outputs an electric pulse when it detects every single photon, the fluorescent intensity can be calculated by counting the number of pulses. In order to ensure the precise positioning of laser focus under large displacement of sample, two translation stages are used simultaneously. One is a two-dimensional (2D) translation stage (Physik Instrumente, PI M-521.DG) with 1 μm resolution. The other is a high-precision three-dimensional (3D) nano translation stage (Physik Instrumente, PI 562.3CD) with 1 nm resolution. The lateral and axial spatial resolution of the system is approximately 180 nm and 800 nm (Hu *et al.* 2022), respectively. To guarantee high positioning resolution and measurement stability, the entire LIFPA system is mounted on a pneumatic isolation optical table.

2.2 Working fluids

In the experiment, 100 μM coumarin 102 (C102, Sigma Aldrich) aqueous solutions of different electric conductivity (σ) and pH values were used in LIFPA measurement, as summarized in Table 1. The C102 solution was prepared with 5% methanol. The thickness of the EDL on the bottom of the channel, which was evaluated by Debye length as

$\lambda = \sqrt{\frac{\epsilon k_B T}{N_A e^2 \sum_i c_i z_i^2}}$, is strictly determined by the solution properties, as shown in Table 1 as well. Here, $\epsilon = \epsilon_0 \epsilon_r$ is electric permittivity with ϵ_r being the relative electric permittivity of water and ϵ_0 being the vacuum permittivity, k_B is Boltzmann constant, T is solution temperature, N_A is Avogadro constant, e is elementary charge, c_i and z_i are the concentration and electric valence of the i^{th} ion.

2.3 Microchip and experimental system of AC EOF

The microchip used in this investigation is diagramed in Figure 2(b). It has a straight microchannel that is 5 mm long (L), 300 μm (w) wide, and 100 μm high (h) as shown in Figure 2(c). The microchip can be divided into three layers and assembled through a layer-by-layer process. (Yang *et al.* 2010) The cover layer is made of an acrylic

Table 1. The pH value, electric conductivity, and the corresponding λ of the fluorescent dye solution used in the experiment

Case	pH	Electric conductivity ($\mu\text{S}/\text{cm}$)	λ (nm)
①	7.11	6.08	42.0
②	7.36	10.43	32.1
③	7.40	14.89	26.3
④	7.58	25.6	20.3
⑤	7.92	41.6	13.1
⑥	8.51	86.0	9.3

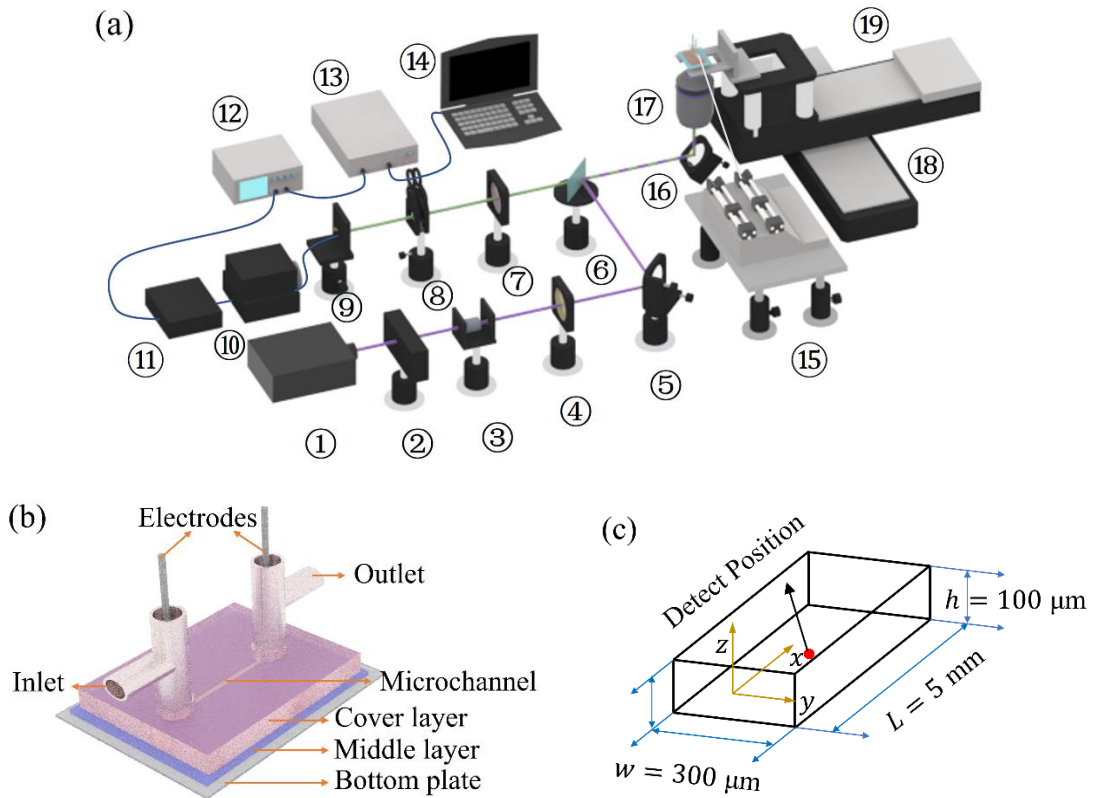


Figure 2 (a) Schematic of the LIFPA system. The system includes (1) 405 nm CW laser; (2) acousto-optic modulator; (3) spatial filter; (4) lens; (5) reflect mirror; (6) dichroic mirror; (7) lens; (8) band-pass filter; (9) band-pass filter and optical fiber connector; (10) PMT; (11) current preamplifier and A/D converter; (12) arbitrary function generator; (13) high voltage amplifier; (14) computer; (15) syringe pump; (16) reflect mirror; (17) objective lens; (18) micrometer translation stage; (19) nanometer piezo translation stage. (b) The schematic of the microchip. (c) The coordinate system and the dimensions of the microchannel.

plate with a thickness of 2 mm. It has good transparency and mechanical strength to support the microchip. The intermediate layer is a channel layer made of plastic sheets. The bottom plate is a 130 μm thick cover slide that has good surface flatness, low fluorescence, and excellent transparency of 405 nm laser.

Two platinum electrodes with a diameter of 100 μm are mounted at the inlet and outlet of the microchannel to generate AC EOF. The AC electric field is supplied by an arbitrary function generator (Tektronix AFG3102C) accompanied by a high voltage amplifier (Trek model PZD700A). In this investigation, the influence of basic flow velocity is taken into account. The basic flow is provided by a syringe pump (HARVARD PUMP 33). Peek tubing is used to connect the syringe pump and the inlet of the microchannel. It can help reduce the flow disturbance induced by tubing deformation or thermal expansion when the basic flow velocity is small.

2.4 Velocity calibration of LIFPA

The LIFPA technique measures flow velocity based on the photobleaching effect of fluorescence. It is well-known that when a fluorescent substance is irradiated with a laser, the fluorescent substance emits fluorescence and is bleached in the meanwhile. When the fluorescent dye is exposed to the laser, the stronger the photobleaching, the weaker the emitted fluorescence. In contrast, the higher the flow velocity of the solution, the shorter the resident time of the fluid within the laser beam, and the weaker the photobleaching. In other words, higher flow velocity causes less photobleaching, which in turn produces a higher intensity of fluorescence. Accordingly, a monotonic relationship between the fluorescent intensity (I_f) and the flow velocity (U) can be established. Based on this relationship, also known as the velocity calibration curve, the flow velocity can be measured by the LIFPA technique. For more details, the readers may refer to Zhao et al. (2016)

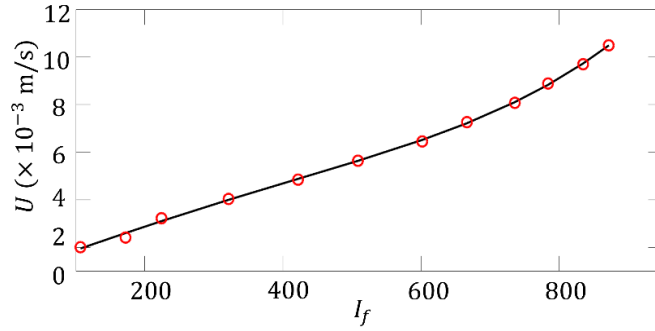


Figure 3 Velocity calibration curve measured at the center of the microchannel. The sampling rate is 1 kHz.

In this investigation, the velocity calibration curve is obtained by measuring the fluorescence intensity at the center of the microchannel in a pressure-driven laminar flow (no electric field was applied), since the flow velocity can be simply calculated. A typical velocity calibration curve is plotted in Figure 3. The $U(I_f)$ relationship is nonlinearly fitted by a 5th order polynomial function. In the subsequent experiments, the velocity of AC EOF adjacent to the EDL of the insulated bottom wall can be directly calculated from the measured I_f through $U(I_f)$.

3. One-dimensional OEOF model

In this investigation, the status of AC EOF on the electrodes is indirectly characterized by the velocity fluctuations of the OEOF induced on insulated wall. This problem can be described generally by Poisson-Nernst-Planck-Navier-Stokes (PNPNS) equations (Hu *et al.* 2020; Hu *et al.* 2022) as

$$\rho_f \left(\frac{\partial \vec{u}}{\partial t} + \vec{u} \cdot \nabla \vec{u} \right) = -\nabla P + \mu \nabla^2 \vec{u} + \rho_e \vec{E} \quad (1)$$

$$\frac{\partial \rho_i}{\partial t} + \vec{u} \cdot \nabla \rho_i = \nabla \cdot b_i z_i \rho_i \vec{E} + D_i \nabla^2 \rho_i \quad (2)$$

$$\rho_e = -\epsilon \nabla \cdot \vec{E} \quad (3)$$

where $\vec{u} = u\vec{x} + v\vec{y} + w\vec{z}$ is the velocity vector, u , v and w represent the magnitude of velocity in x , y and z directions. ρ_f is the density of fluid, P is pressure, μ is dynamic viscosity, ε is electric permittivity of fluid, $\rho_e = \sum_i \rho_i z_i$ is net charge density, with ρ_i , b_i , z_i and D_i being the density, mobility, valence and diffusivity of the i^{th} ion, respectively. $\vec{E} = E_x\vec{x} + E_y\vec{y} + E_z\vec{z}$ is the electric field vector, with E_x , E_y and E_z being the electric field components in x , y and z directions, respectively. Besides, considering the fluid is incompressible, $\nabla \cdot \vec{u} = 0$.

In this investigation, the direction of fluid movement and the direction of the electric field are both parallel to the x -axis. Since we focus on the transition of AC EOF from linear to nonlinear status, the electric field is not sufficiently strong to induce two- and three-dimensional ICEO near the electrodes. Therefore, a 1D approximation (Hu *et al.* 2020; Hu *et al.* 2022) of the electric field can be applied to this model. The physical quantities in the equations above can be analyzed by the following dimensions

$$t = t^*/f_f, \quad x = x^*l_0, \quad y = y^*\lambda, \quad u' = u'^*U_0, \quad P' = P'^*\rho_f U_0^2, \quad \rho_i = \rho_i^*\rho_{i0}, \quad E = E^*E_A, \\ \rho_{e,1} = -\varepsilon V_T/\lambda^2 \rho_{e,1}^*, \quad \rho_{e,2} = -\varepsilon|\zeta|/\lambda^2 \rho_{e,2}^*, \quad \frac{\partial E_x}{\partial x} \sim \frac{V_T}{l_0^2} \frac{\partial E^*}{\partial x^*} \quad (4)$$

where l_0 is a characteristic large scale, U_0 is a characteristic velocity, E_A is the amplitude of the external electric field with $E_A = V_{ext}/L$ and V_{ext} is the amplitude of the external AC voltage across the electrodes. $\rho_{e,1}$ and $\rho_{e,2}$ are the electric charge density on the surface of electrode and insulated wall, respectively. ζ is zeta potential on the insulated bottom. $V_T = k_B T/e$ is thermal potential.

The selection of U_0 is crucial to characterize AC EOF. Previously, the most commonly used format of U_0 is according to Helmholtz-Smoluchowski velocity $U_{HS} = \varepsilon\zeta E_A/\mu$ (Bazant & Squires 2004; Dutta & Beskok 2001; Hojgaard Olesen *et al.* 2010; Park & Lee 2008; Rubin *et al.* 2016; Zhao & Yang 2013). However, as discussed in a recent paper (Hu *et al.* 2021), U_{HS} is intrinsically an electro-viscous velocity which leads to overcounting of viscosity if applied in Reynolds number. Besides, U_{HS} cannot reveal the crucial roles of AC frequency and ion concentration on the velocity fluctuations of OEOF. For these reasons, in contrast to our previous investigation (Hu *et al.* 2022), we suggest using an electro-inertial velocity $U_0 = \varepsilon k_B T E_A / e \lambda^2 \rho_f f_f$ (Hu *et al.* 2021) to characterize the velocity fluctuations of OEOF. When the applied AC electric field is insufficiently strong to induce chaotic flow, we can certainly neglect the nonlinear term of u' ($= u - \bar{u}$ with \bar{u} being mean flow velocity and $\bar{\cdot}$ represent temporal averaging). Let $\rho_i'^* = 1 - \rho_i^*$ being the dimensionless ion density fluctuation, accordingly, the dimensionless forms of Eqs. (1)-(3) with 1D electric field approximation become

$$\frac{k_B T}{e|\zeta|} \frac{\partial u'^*}{\partial t^*} = -\frac{k_B T U_0}{e f_f |\zeta| l_0} \frac{\partial p'^*}{\partial x^*} + \mu \frac{k_B T}{e|\zeta| \lambda^2 \rho_f f_f} \frac{\partial^2 u'^*}{\partial y^{*2}} + \rho_e^* E^* \quad (5)$$

$$\frac{f_f l_0^2}{D_i} \frac{\partial \rho_i'^*}{\partial t^*} + \left(\frac{\bar{u}}{U_0} + u'^* \right) \frac{U_0 l_0}{D_i} \frac{\partial \rho_i'^*}{\partial x^*} = \frac{b_i z_i E_A l_0}{D_i} E^* \frac{\partial \rho_i'^*}{\partial x^*} + \frac{b_i z_i E_A l_0}{D_i} (1 + \rho_i'^*) \frac{\partial E^*}{\partial x^*} + \frac{\partial^2 \rho_i'^*}{\partial x^{*2}} \quad (6)$$

$$\frac{\varepsilon V_T}{2\lambda^2} (\rho_+'^* - \rho_-'^*) = -\varepsilon \frac{V_T}{l_0^2} \frac{\partial E^*}{\partial x^*} \quad (7)$$

Furthermore, considering Nernst-Einstein equation $D_i = b_i k_B T / z_i e$, Eq. (6) can be rewritten as

$$\frac{f_f l_0^2}{D_i} \frac{\partial \rho_i'^*}{\partial t^*} + \left(\frac{\bar{u}}{U_0} + u'^* \right) \frac{U_0 l_0}{D_i} \frac{\partial \rho_i'^*}{\partial x^*} = \frac{z_i^2 e E_A l_0}{k_B T} E^* \frac{\partial \rho_i'^*}{\partial x^*} + \frac{z_i^2 e E_A l_0}{k_B T} (1 + \rho_i'^*) \frac{\partial E^*}{\partial x^*} + \frac{\partial^2 \rho_i'^*}{\partial x^{*2}} \quad (8)$$

From Eq. (7), it is easily seen

$$\rho_+'^* - \rho_-'^* = -\frac{2\lambda^2}{l_0^2} \frac{\partial E^*}{\partial x^*} \quad (9)$$

For the sake of simplicity, we consider a simple binary symmetric electrolyte. The positive and negative ions have equivalent magnitude of valence ($z_+ = -z_- = z$) and accordingly $z_+^2 = z_-^2 = z^2$. By combing Eq. (8) and (9), it is simply obtained

$$\begin{aligned} & \left(\frac{f_f l_0^2}{D_+} \frac{\partial \rho_+^{I*}}{\partial t^*} - \frac{f_f l_0^2}{D_-} \frac{\partial \rho_-^{I*}}{\partial t^*} \right) + \left(\frac{\bar{u}}{U_0} + u'^* \right) \left(\frac{U_0 l_0}{D_+} \frac{\partial \rho_+^{I*}}{\partial x^*} - \frac{U_0 l_0}{D_-} \frac{\partial \rho_-^{I*}}{\partial x^*} \right) \\ & = \frac{z^2 e E_A l_0}{k_B T} E^* \frac{\partial}{\partial x^*} \left(-\frac{2\lambda^2}{l_0^2} \frac{\partial E^*}{\partial x^*} \right) + \frac{z^2 e E_A l_0}{k_B T} \frac{\partial E^*}{\partial x^*} \left(-\frac{2\lambda^2}{l_0^2} \frac{\partial E^*}{\partial x^*} \right) + \frac{\partial^2}{\partial x^{*2}} \left(-\frac{2\lambda^2}{l_0^2} \frac{\partial E^*}{\partial x^*} \right) \end{aligned} \quad (10a)$$

$$\frac{\partial}{\partial t^*} (\rho_+^{I*} - \rho_-^{I*}) = -\frac{2\lambda^2}{l_0^2} \frac{\partial}{\partial t^*} \frac{\partial E^*}{\partial x^*} \quad (10b)$$

$$\frac{\partial}{\partial x^*} (\rho_+^{I*} - \rho_-^{I*}) = -\frac{2\lambda^2}{l_0^2} \frac{\partial}{\partial x^*} \frac{\partial E^*}{\partial x^*} \quad (10c)$$

In the Eqs. (10a-c), there are five unknowns (e.g. $\frac{\partial \rho_+^{I*}}{\partial t^*}$, $\frac{\partial \rho_-^{I*}}{\partial t^*}$, $\frac{\partial \rho_+^{I*}}{\partial x^*}$, $\frac{\partial \rho_-^{I*}}{\partial x^*}$ and E^*) but three equations. The equations are non-closure. Thus, we further assume the positive and negative have equivalent D_i with $D_+ \approx D_- = D$. After this approximation, Eqs. (5), (10a) and (9) can be simplified as

$$\frac{\partial u'^*}{\partial t^*} = -\frac{1}{Sr} \frac{\partial p'^*}{\partial x^*} + \frac{1}{St} \frac{\partial^2 u'^*}{\partial y^{*2}} + \frac{1}{\kappa} \rho_e^* E^* \quad (11a)$$

$$StSc\gamma^2 \frac{\partial}{\partial t^*} \left(\frac{\partial E^*}{\partial x^*} \right) + P_{e,EOF} (\beta + u'^*) \frac{\partial}{\partial x^*} \left(\frac{\partial E^*}{\partial x^*} \right) = P_{e,EP} E^* \frac{\partial}{\partial x^*} \left(\frac{\partial E^*}{\partial x^*} \right) + P_{e,EP} \frac{\partial E^*}{\partial x^*} \left(\frac{\partial E^*}{\partial x^*} \right) + \frac{\partial^2}{\partial x^{*2}} \left(\frac{\partial E^*}{\partial x^*} \right) \quad (11b)$$

$$\frac{\gamma^2}{2} (\rho_+^{I*} - \rho_-^{I*}) = -\frac{\partial E^*}{\partial x^*} \quad (11c)$$

where $St = \lambda^2 \rho_f f_f / \mu$ being the Stokes number for oscillating flows, $Sr = f_f l_0 / U_0$ is Strouhal number, $\kappa = k_B T / e |\zeta|$ is a ratio between thermal potential and zeta potential, $Sc = \mu / \rho_f D$ is Schmidt number, $\gamma = l_0 / \lambda$ is an aspect ratio between the large scale and EDL scale, $\beta = \bar{u} / U_0$ is a velocity ratio between the mean flow velocity and U_0 , $P_{e,EOF} = U_0 l_0 / D = \varepsilon E_A l_0 z_i / \lambda^2 \rho_f f_f b_i$ is the Peclet number for EOF, $P_{e,U} = \bar{u} l_0 / D$ is the Peclet number of the local mean flow velocity and $P_{e,EP} = z^2 e E_A l_0 / k_B T$ is the Peclet number of electrophoresis.

If we further consider small velocity fluctuations, i.e. $|u'^*| \ll \beta$, and all the magnitudes of $StSc\gamma^2$, $P_{e,U} = P_{e,EOF} \beta = \bar{u} l_0 / D$ (Peclet number related to the local mean flow velocity), $P_{e,EP}$ in Eq. (11b) are much larger than unity, Eq. (11b) can be simplified as

$$StSc\gamma^2 \frac{\partial}{\partial t^*} \left(\frac{\partial E^*}{\partial x^*} \right) + P_{e,U} \frac{\partial}{\partial x^*} \left(\frac{\partial E^*}{\partial x^*} \right) = P_{e,EP} E^* \frac{\partial}{\partial x^*} \left(\frac{\partial E^*}{\partial x^*} \right) + P_{e,EP} \frac{\partial E^*}{\partial x^*} \left(\frac{\partial E^*}{\partial x^*} \right) \quad (12)$$

After integrating Eq. (12) over x^* , it becomes

$$StSc\gamma^2 \frac{\partial E^*}{\partial t^*} + P_{e,U} \frac{\partial E^*}{\partial x^*} - \frac{P_{e,EP}}{2} \frac{\partial E^{*2}}{\partial x^*} = g(t^*) \quad (13)$$

Thus, after dimensional analysis, the Nernst-Planck equation (Eq. (6)) is turned into Eq. (13) which is a perturbed inviscid Burger's equation of electric field with the presence of external forcing term. If the external electric field is sinusoidal, e.g. $E_{ext} = E_A \sin(2\pi f_f t)$, we have $g(t^*) = 2\pi StSc\gamma^2 \cos(2\pi t^*)$. Eq. (13) can be rewritten as

$$\frac{\partial E^*}{\partial t^*} + \frac{P_{e,U}}{StSc\gamma^2} \frac{\partial E^*}{\partial x^*} - \frac{P_{e,EP}}{2StSc\gamma^2} \frac{\partial E^{*2}}{\partial x^*} = 2\pi \cos(2\pi t^*) \quad (14)$$

From Eq. (11a), when the f_f is smaller than the response frequency of EDL on insulated bottom wall, we approximately have $u'^* = -Z_f E^*$, with $Z_f = St / \kappa$. Then, after substituting $E^* = -u'^* / Z_f$ into Eq. (14), it is obtained

$$\frac{\partial u'^*}{\partial t^*} + Z_l \frac{\partial u'^*}{\partial x^*} + Z_{nl} \frac{\partial u'^{*2}}{\partial x^*} = -2\pi Z_f \cos(2\pi t^*) \quad (15)$$

where $Z_l = \frac{P_{e,U}}{StSc\gamma^2} = \frac{\bar{u}}{f_f l_0}$ and $Z_{nl} = \frac{P_{e,EP}}{2StSc\gamma^2 Z_f} = \frac{z^2 E_A \mu D}{2|\zeta| \lambda^2 \rho_f f_f^2 l_0}$ are the coefficients of linear and nonlinear terms respectively. Eq. (15) is different from previous investigations (Hu *et al.* 2022) where the characteristic velocity was

U_{HS} . The nonlinear term coefficient Z_{nl} and the forcing term coefficient Z_f provides more information about zeta potential, ion concentration (through λ) and even pH value. This is exactly what we desired in this investigation.

4. Experimental results and discussions

4.1 Statistics of the velocity field

1) Mean velocity

The mean velocity \bar{u} at different frequencies and different flow rates Q are measured first, as shown in Figure 4. In the unforced case where $f_f = 0$ Hz, \bar{u} varies with Q in an approximately linear manner as expected. When the AC electric field is applied, \bar{u} at different AC frequencies just has a negligibly small derivation from the counterpart of the unforced case. This result indicates that in the considered ranges of frequency and intensity of the AC electric field, the applied AC electric field has little effect on the mean velocity of the flow. No detectable mean flow has been induced according to the AC EOF.

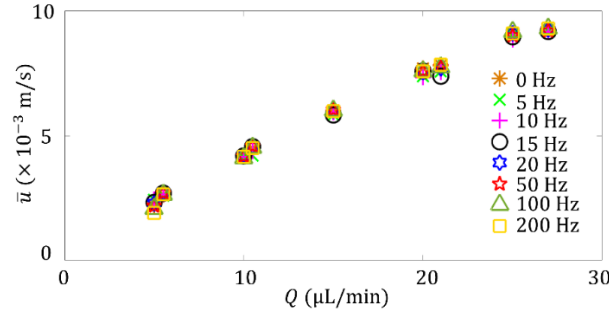


Figure 4 Relationship between flow rate Q and mean velocity \bar{u} at different AC frequencies, where $E_A = 8 \times 10^4$ V/m. Here, $\sigma = 6.08$ $\mu\text{S/cm}$ and $\text{pH} = 7.11$. The sampling rate is 1 kHz.

2) Velocity fluctuations driven by AC electric field

The velocity fluctuations has been evaluated by the root mean square of u' , as $u_{rms} = \sqrt{u'^2}$. First, the influence of E_A on u_{rms} under the different Q and f_f is plotted in Figure 5(a-b). Under lower $Q = 10.5$ $\mu\text{L/min}$, u_{rms} first increases linearly with E_A , and then reaches a nonlinear regime when E_A is over a transitional value (say $E_{A,C}$). The phenomenon is more visible at lower f_f . When $f_f \geq 50$ Hz, the nonlinear regime of the u_{rms} versus E_A curve becomes indistinguishable. The nonlinearity of AC EOF has been inhibited by the increased f_f . This is predictable from Eq. (15), where the coefficient of linear term $Z_l \sim f_f^{-1}$, while the coefficient of nonlinear term $Z_{nl} \sim f_f^{-2}$. As f_f is increased, the influence of the nonlinear term decreases faster than the linear term, which in turn, leads to a relatively stronger influence of the linear term on AC EOF. When Q is increased to 27 $\mu\text{L/min}$, even under lower f_f , the nonlinear regime of u_{rms} versus E_A curve is almost invisible. The results further indicate linearity of AC EOF is enhanced by increasing Q , which is also consistent with the prediction that $Z_l \sim \bar{u}$.

The influence of E_A on u_{rms} can be moved distinguishable from the plots of Z_{nl} vs u_{rms}/U_0 in Figure 5(c-d). It is obvious that at a lower Z_l (e.g. $Q = 10.5$ $\mu\text{L/min}$ in Figure 5(c)), u_{rms}/U_0 exhibits transitions from a linear regime (with $u_{rms}/U_0 \sim Z_{nl}^0$) to a nonlinear regime (with $u_{rms}/U_0 \sim Z_{nl}^\alpha$ and $\alpha < 0$) with increasing Z_{nl} when f_f is relatively lower (e.g. $f_f \leq 50$ Hz), according to the relatively large Z_{nl} and stronger nonlinearity of AC EOF.

The smaller the f_f , the smaller the α in the nonlinear regime is. α asymptotically approaches $-1/2$. In contrast, at a larger Z_l (e.g. $Q = 27 \mu\text{L}/\text{min}$ in Figure 5(d)), the nonlinear regime is not observed.

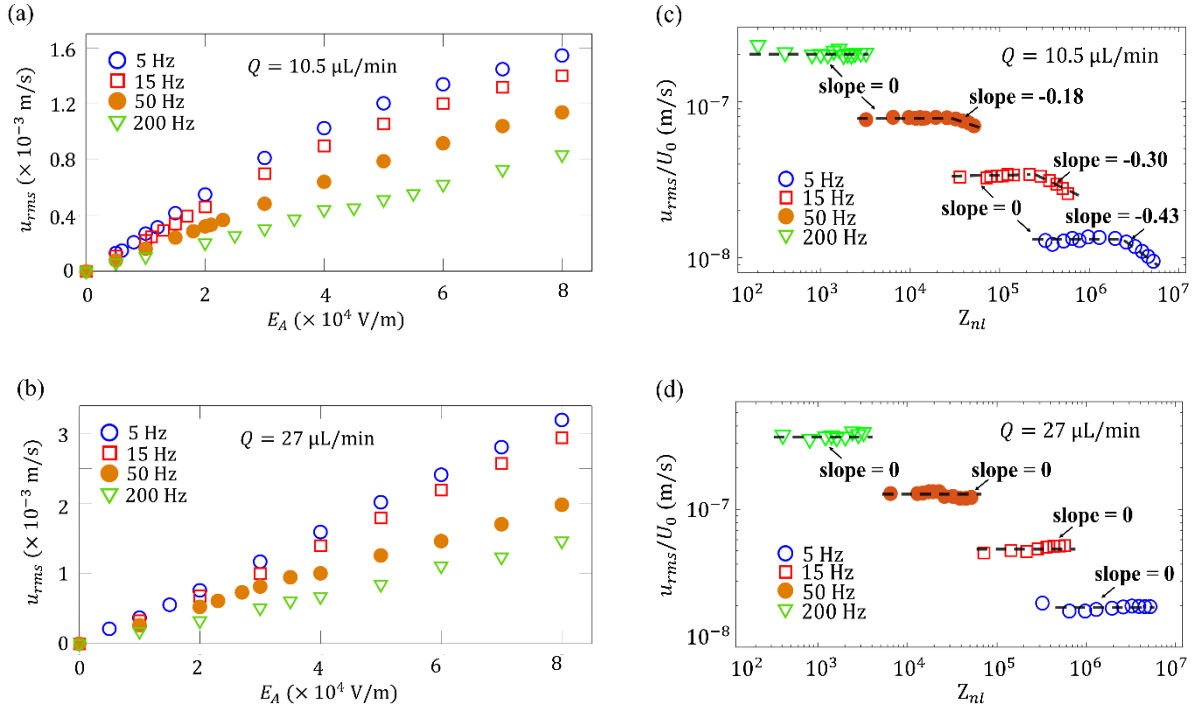


Figure 5 (a-b) Relationship between u_{rms} and E_A at different f_f . The sampling rate is 1 kHz. Here, $\sigma = 6.08 \mu\text{S}/\text{cm}$ and $\text{pH} = 7.11$. (a) $Q = 10.5 \mu\text{L}/\text{min}$; (b) $Q = 27 \mu\text{L}/\text{min}$. (c-d) Relationship between u_{rms}/U_0 and Z_{nl} at different E_A and f_f corresponding to (a-b). (c) $Q = 10.5 \mu\text{L}/\text{min}$; (d) $Q = 27 \mu\text{L}/\text{min}$.

The influence of Q on u_{rms} curve can be more visible from Figure 6(a-b). Under $f_f = 10$ Hz as shown in Figure 6(a), in the considered range of E_A , there is always a nonlinear regime when $Q \leq 15 \mu\text{L}/\text{min}$. When $Q > 15 \mu\text{L}/\text{min}$, the nonlinear regime is beyond the range of E_A in this investigation. In the meanwhile, accompanied with

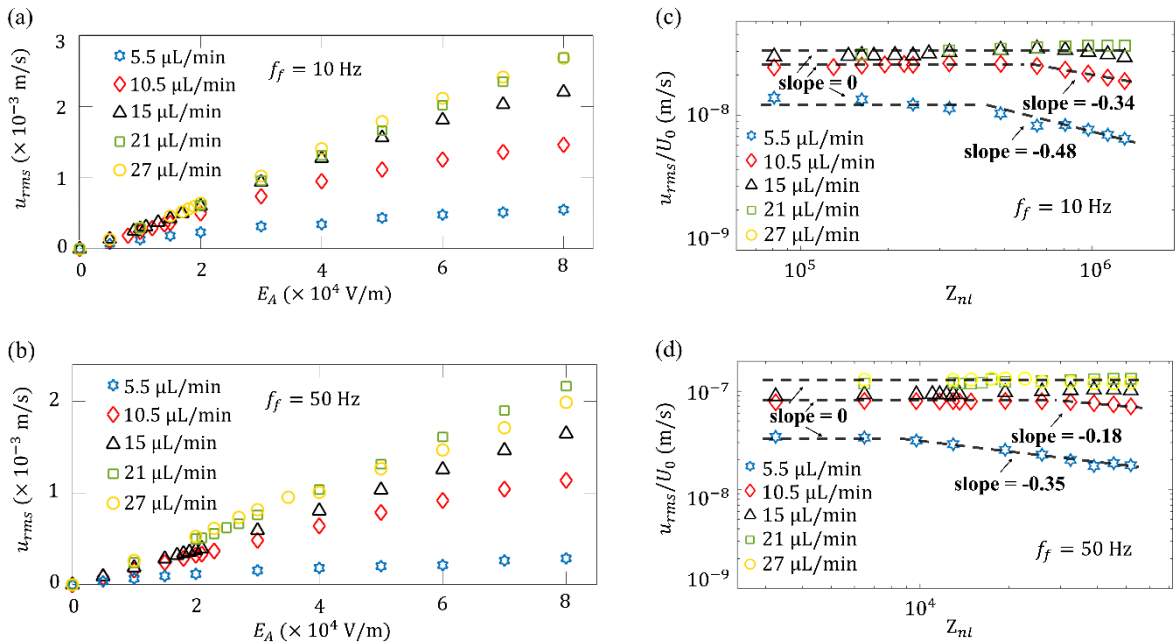


Figure 6 (a-b) Relationship between u_{rms} and E_A at different Q . The sampling rate is 1 kHz. Here, $\sigma = 6.08$ $\mu\text{S}/\text{cm}$ and $\text{pH} = 7.11$. (a) $f_f = 10$ Hz, and (b) $f_f = 50$ Hz. (c-d) Relationship between u_{rms}/U_0 and Z_{nl} at different E_A and Q corresponding to (a-b). (c) $f_f = 10$ Hz, and (d) $f_f = 50$ Hz.

the increasing Q , u_{rms} gradually increases. Similar results can further be found in Figure 6(b) where $f_f = 50$ Hz. From Figure 6(c), it can be seen the width of the linear regime apparently increases with Q , and Z_l as well. Accordingly, the nonlinear regime becomes narrower with larger α , indicating the inhibition of nonlinearity of AC EOF by Q . The difference is, as shown in Figure 6(c, d), the nonlinear regime is postponed due to the higher f_f .

The influence of Q on u_{rms} in both the linear and nonlinear regimes of AC EOF can be further shown in Figure 7(a-b). The trend u_{rms} gradually increases with Q is more clearly observed for all f_f and E_A . In the meanwhile, the dimensionless velocity u_{rms}/U_0 is also increasing with Z_l (Figure7(c-d)). Figure 5-7 reflects the influence of E_A , Q and f_f on u_{rms} from different aspects, which is coincident with the investigation of Hu et al (2022). These parameters have a significant influence on the linearity and nonlinearity of AC EOF, which could be properly elucidated by Z_l and Z_{nl} in Eq. (15).

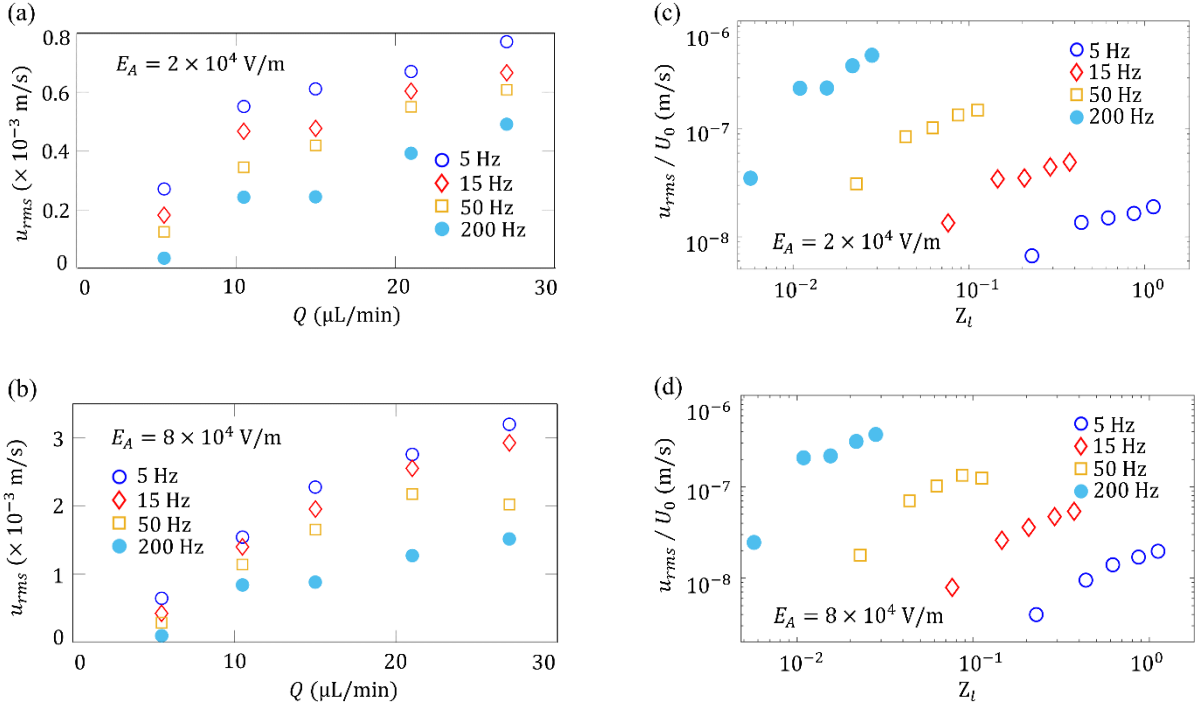


Figure 7 (a-b) Relationship between u_{rms} and Q at different f_f . The sampling rate is 1 kHz. Here, $\sigma = 6.08$ $\mu\text{S}/\text{cm}$ and $\text{pH} = 7.11$. (a) $E_A = 2 \times 10^4$ V/m; (b) $E_A = 8 \times 10^4$ V/m. (c-d) Relationship between u_{rms}/U_0 and Z_l at different Q and f_f corresponding to (a-b). (c) $E_A = 2 \times 10^4$ V/m; (d) $E_A = 8 \times 10^4$ V/m.

4.2 Time series of velocity fluctuations

1) Time series of velocity fluctuations vary with E_A

The transient velocity fluctuations can be more straight-forwardly observed by the time series of u^{**} . In this section, the influence of E_A on the status of AC EOF is studied first. Considering E_A is linearly related to Z_{nl} , it is equivalent to studying the influence of Z_{nl} on the time series of u^{**} . Here, the time series of u^{**} at $f_f = 5$ Hz and $Q = 10.5$ $\mu\text{L}/\text{min}$ are plotted as examples.

In Figure 8(a), it can be seen the time series of u'^* changes as E_A is increased. When $E_A = 5 \times 10^3$ V/m, the time series of u'^* is symmetric on time and coincident with a sinusoidal waveform from the AC electric field. Apparently, the AC EOF is in a linear regime. When E_A is increased to 4×10^4 V/m, compared with the applied sinusoidal AC electric field, the waveforms of the time series become asymmetric with unbalanced peak and trough values. This indicates that the nonlinear behavior of AC EOF begins to affect the time series of u'^* . As E_A is further increased to 8×10^4 V/m, the amplitude of the time series is significantly inhibited relative to the lower E_A counterparts, since the time series apparently departs the applied sinusoidal AC electric field. From the time series of u'^* , it is easier to distinguish the linear and nonlinear status of AC EOF. In the linear regime of AC EOF, u'^* has unchanged amplitude with increasing E_A and symmetric time series on t^* , while in the nonlinear regime of AC EOF, u'^* has decreasing amplitude with E_A and asymmetric time series on t^* .

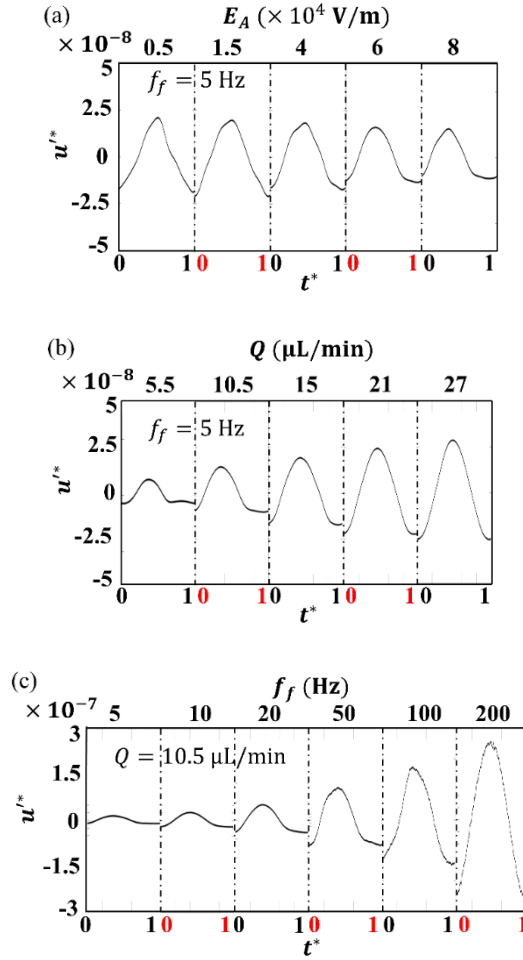


Figure 8 Time series of u'^* at different conditions, sampling rate is 1 kHz. Here, $\sigma = 6.08$ $\mu\text{S}/\text{cm}$ and $\text{pH} = 7.11$. For each case, only one period of u'^* is plotted. (a) u'^* vs E_A , where $Q = 10.5$ $\mu\text{L}/\text{min}$ and $f_f = 5$ Hz. (b) u'^* vs Q , where $E_A = 8 \times 10^4$ V/m and $f_f = 5$ Hz. (c) u'^* vs f_f , where $E_A = 8 \times 10^4$ V/m and $Q = 10.5$ $\mu\text{L}/\text{min}$.

2) Time series of velocity fluctuations vary with Q

In Figure 4, Q is monotonically related to the local mean flow velocity \bar{u} and determines Z_l only. Since increased Q can enhance the linearity and inhibit the nonlinearity of AC EOF, to reveal the transition of AC EOF between linear and nonlinear status along Q in a more clear way, we selected a large $E_A = 8 \times 10^4$ V/m and small

AC frequency $f_f = 5$ Hz in this section. As shown in Figure 8(b), the time series of u'^* with $Q = 5.5$ $\mu\text{L}/\text{min}$ is highly asymmetrical. The flow is highly nonlinear where a slight protrusion related to the “turn-over” of flow (Hu *et al.* 2020) can be found at the trough. When Q is increased to 10.5 $\mu\text{L}/\text{min}$, the protrusion gradually disappeared accompanied with less asymmetry of the time series of u'^* . As Q is further increased from 15 to 27 $\mu\text{L}/\text{min}$, the asymmetry of the time series of u'^* continuously decreases with the peak height increases. The waveform returns into a standard sinusoidal waveform, indicating the nonlinearity is continuously weakened and the linear regime is recovered. Again, from the time series of u'^* , it is supported that the increased Q inhibits the generation of nonlinear AC EOF, as a result of the increasing Z_l .

3) Time series of velocity fluctuations vary with f_f

The effect of AC frequency f_f on the time series of u'^* is more complicated. As can be seen in Eq. (15), when f_f is changed, $Z_l \sim f_f^{-1}$, $Z_{nl} \sim f_f^{-2}$ and $Z_f \sim f_f$ are all changed. Here, we only show the experimental results at $E_A = 8 \times 10^4$ V/m and $Q = 10.5$ $\mu\text{L}/\text{min}$. In Figure 8(c), it can be clearly observed that as f_f is increased, the time series of u'^* shows less asymmetry, and more sinusoidal with their peak values increased. This can be attributed to $U_0 \sim f_f^{-1}$ while $u_{rms} \sim f_f^{-\alpha}$ with $\alpha < 1$ qualitatively (Zhao *et al.* 2018). Thus, u'^* has an increasing relationship with the AC frequency as $f_f^{1-\alpha}$. Figure 8(c) indicates, the higher the frequency, the more difficult for AC EOF to transition to nonlinear status.

From the results of the time series, it can be clearly seen that the status of AC EOF is determined by the three control parameters: E_A , f_f , and Q (or local mean flow velocity \bar{u} equivalently). Their influence can be summarized in the following: (1) the larger the E_A , the stronger the nonlinearity of AC EOF, and the more asymmetric the time series of velocity fluctuations; (2) the higher the f_f , the weaker the nonlinearity of AC EOF, and the less asymmetric the time series of velocity fluctuations; (3) the greater the Q , the weaker the nonlinearity of AC EOF, and the less asymmetric the time series of velocity fluctuations. From the experimental results above, it can be seen when the nonlinearity of AC EOF is weak (i.e. Z_{nl} is sufficiently small), it is difficult to distinguish the linear and nonlinear status of AC EOF through the time series of velocity fluctuations. This is an obstacle to revealing the transition between the linear and nonlinear status of AC EOF.

4.3 Velocity power spectrum under different conditions

The intrinsic difference between the linear and nonlinear AC EOF is the response of the internal electric field and the corresponding EOF velocity relative to the external AC electric field. The linear AC EOF responds linearly to an external electric field, while the nonlinear one responds nonlinearly to an external electric field with waveform distortion, as theoretically predicted by Olesen *et al.* (2010) In other words, in nonlinear AC EOF, the velocity power spectrum of u' could have different aspects than the external AC electric field. Therefore, according to the criterion of distinguishing linear and nonlinear regimes defined by Hu *et al.* (2022), the velocity power spectrum ($S(f)$) of u' is studied to achieve an in-depth analysis on the status of AC EOF. For convenience, the results are plotted by a dimensionless frequency $f^* = f/f_f$.

1) $S(f)$ varies with E_A

In the experiment, the power spectrum of velocity fluctuations at five different flow rates were measured at different electric field strengths and frequencies. The noise level is plotted by the dashed lines.

In Figure 9(a), a sinusoidal AC signal with $f_f = 5$ Hz is applied to the system. The E_A gradually increases from 5×10^3 to 8×10^4 V/m. At $E_A = 5 \times 10^3$ V/m, there is only a single peak observed in the velocity power spectrum at $f^* = 1$, indicating the EOF behaves linearly to the applied AC electric field. As E_A is increased to

1×10^4 V/m, two peaks appear in the power spectrum at the positions of $f^* = 1$ and 2. The appearance of high-order harmonics at $f^* = 2$ indicates the AC EOF transits into a nonlinear regime. When $E_A = 2 \times 10^4$ V/m, more peaks appear in the power spectrum at the positions of $f^* = 1, 2$ and 3. At the same time, a new peak appears at $f^* = 1.2$ as a sideband of the AC frequency. Subsequently, as E_A gradually increases from 2×10^4 V/m to 8×10^4 V/m, more peaks corresponding to the harmonic and subharmonic (e.g. $f^* = 0.8$) frequencies emerge. The peak value at $f^* = 1$ reaches saturation when $E_A = 4 \times 10^4$ V/m, as can be observed from Figure 9(c). While the peak values at harmonic frequencies increase rapidly, indicating increasing nonlinearity. Although the peak values decrease with f^* generally, one interesting phenomenon is, occasionally, the peak values at odd f^* can be even

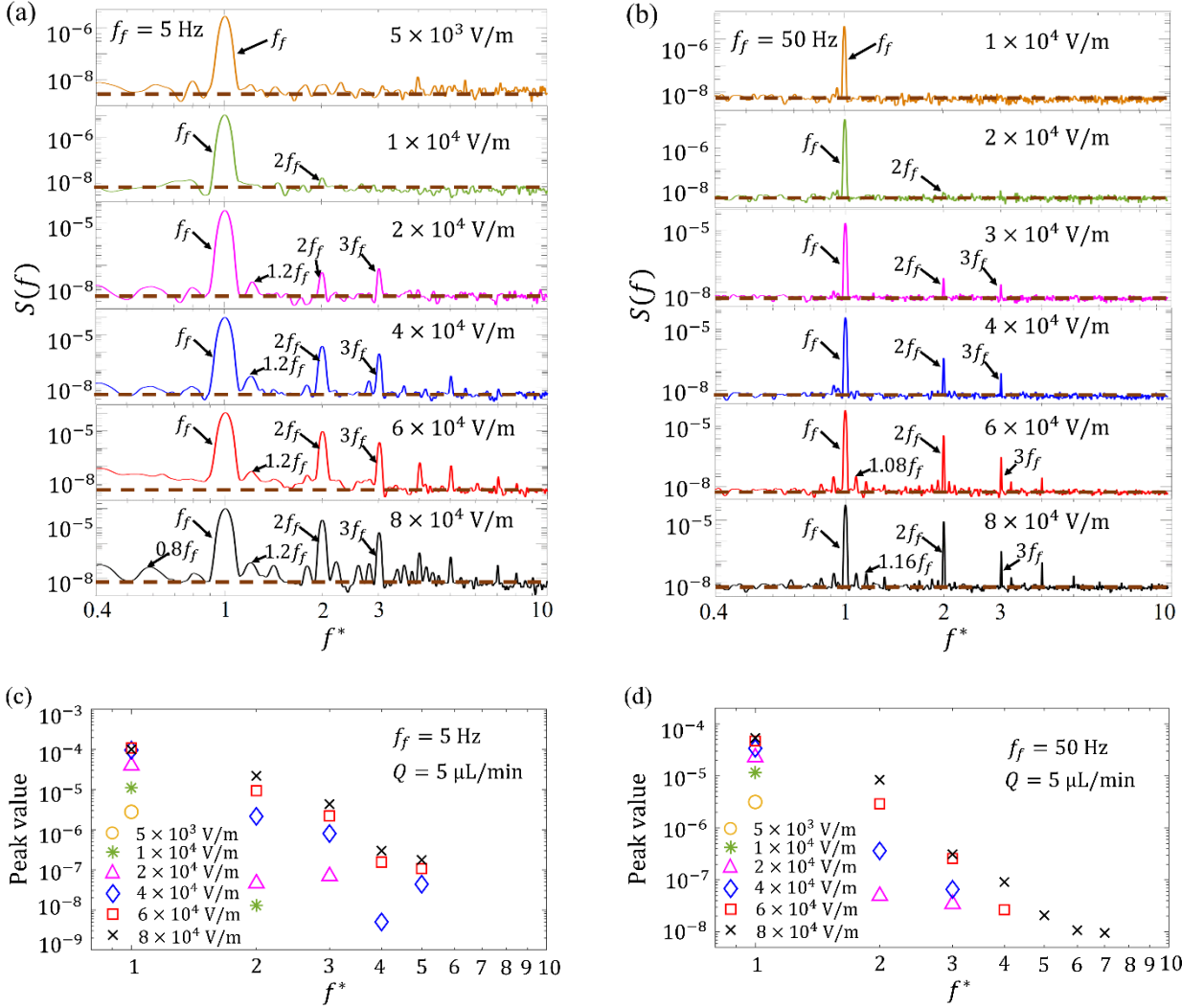


Figure 9 (a-b) Power spectrum of u' under different E_A , the sampling rate is 1 kHz. Here, $\sigma = 6.08 \mu\text{S}/\text{cm}$, $\text{pH} = 7.11$, $Q = 5 \mu\text{L}/\text{min}$. The dashed lines indicate the noise level of unforced flow. (a) $f_f = 5$ Hz, (b) $f_f = 50$ Hz. (c-d) Peak values of $S(f)$ at different f^* . (c) $f_f = 5$ Hz, (d) $f_f = 50$ Hz.

higher than that at the neighboring even f^* . For instance, when $E_A = 2 \times 10^4$ V/m, $f^* = 3$ exhibits a larger peak value than that of $f^* = 2$, indicating a potential influence of low-frequency long-wave interaction in Eq. (15). This might be attributed to a resonance between the AC electric field and the RC dynamics, which has a characteristic RC frequency of $f_{RC} \approx 5$ Hz (Bazant *et al.* 2004). The growth of peak values at the odd-order harmonic frequencies is significantly enhanced, while those of even-order frequencies are slightly inhibited.

When $f_f = 50$ Hz and the E_A gradually increases from 1×10^4 to 8×10^4 V/m (Figure 9(b)), similar phenomena have been observed. There are two major differences from the low f_f counterpart. One is that the $S(f)$

at the lower f_f shows more spectral components (i.e. peaks) than that at the higher f_f . The other is the subharmonic frequencies at $f_f = 50$ Hz locate at $f^* = 1.08$ and 1.16 etc, which are different from that at $f_f = 5$ Hz. These results are also different from the previous investigations (Hu *et al.* 2020; Hu *et al.* 2021; Hu *et al.* 2022) in AC EOF and other EK systems (Shi *et al.* 2023). Especially, the chaotic state observed by Hu *et al.* (2021) has not been observed even though E_A is sufficiently high. From the physical point of view, this is not good news, since the physical problem is highly specific, may be attributed to different bifurcation or resonant interaction mechanisms, and may lack of universality. Besides, in Figure 9(d), the phenomenon that the peak values at odd f^* (eg. $f^* = 3$) can be occasionally higher than that at the neighboring even f^* (eg. $f^* = 2$) is not observed in this case.

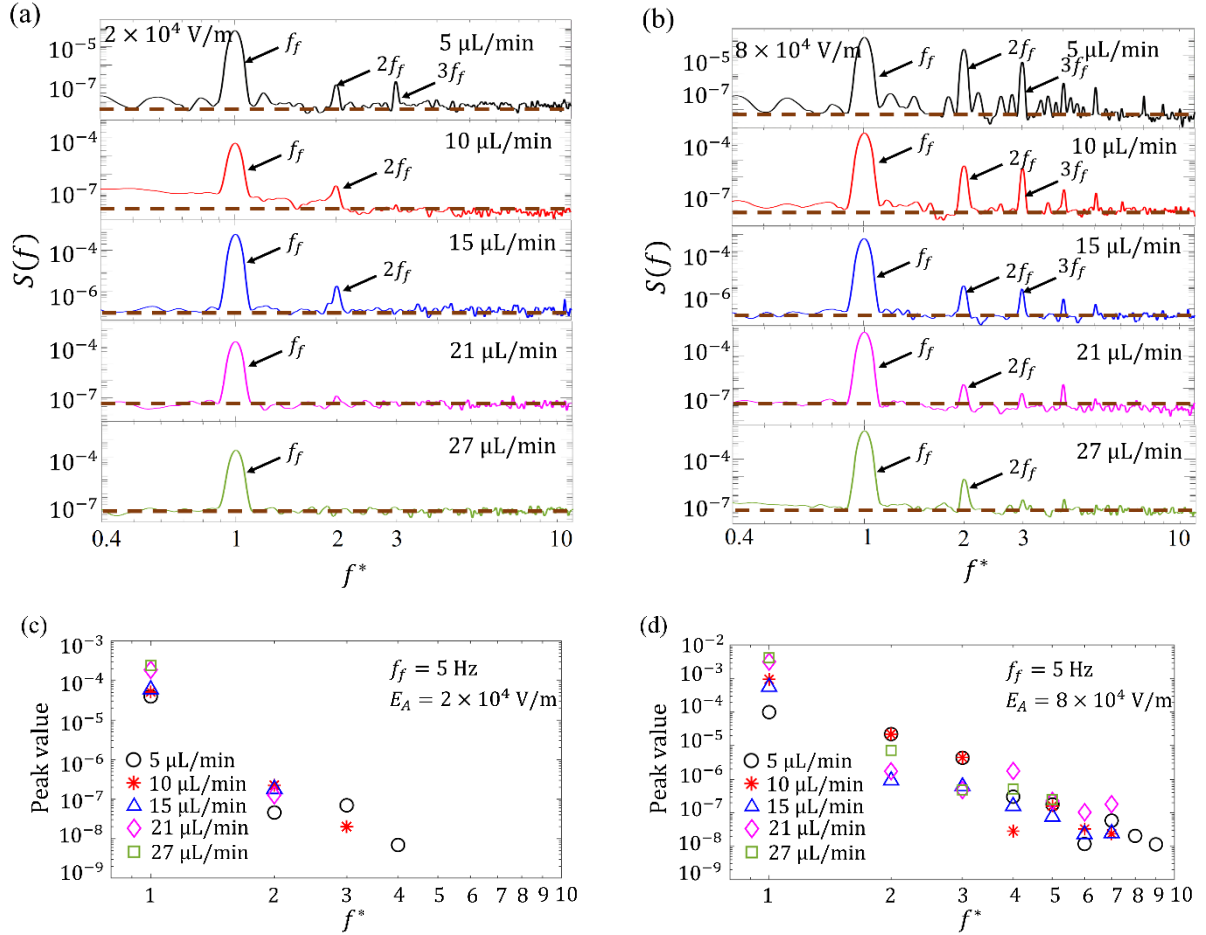


Figure 10 (a-b) Power spectrum of u' under different Q , where $f_f = 5$ Hz. The sampling rate is 1 kHz. Here, $\sigma = 6.08$ $\mu\text{S}/\text{cm}$ and $\text{pH} = 7.11$. The dashed lines indicate the noise level of the unforced flow. (a) $E_A = 2 \times 10^4$ V/m, (b) $E_A = 8 \times 10^4$ V/m. (c-d) Peak values of $S(f)$ at different E_A . (c) $E_A = 2 \times 10^4$ V/m, (d) $E_A = 8 \times 10^4$ V/m.

2) $S(f)$ of u' varies with Q

The influence of Q on the nonlinearity of AC EOF can also be directly observed in spectral space. At $E_A = 2 \times 10^4$ V/m (Figure 10(a)), when $Q = 5$ $\mu\text{L}/\text{min}$, $S(f)$ of u' has a series of peaks at $f^* = 1, 2$ and 3 , proving that both the linear and nonlinear behavior coexist at this time. When Q increases to 10 $\mu\text{L}/\text{min}$, only two peaks remain at $f^* = 1$ and 2 . As Q gradually increases to 27 $\mu\text{L}/\text{min}$, $S(f)$ only has a single peak at $f^* = 1$. All the peaks at the higher-order harmonic frequencies disappear. The nonlinear behavior is absent and the AC EOF returns to a linear regime.

The trend can be more visible at $E_A = 8 \times 10^4$ V/m, as shown in Figure 10(b). When $Q = 5$ $\mu\text{L}/\text{min}$, beyond $f^* = 1$, many spikes have been observed at the harmonics, subharmonics, and other components of f_f , indicating the AC EOF is in a nonlinear regime. As Q increases from 5 to 27 $\mu\text{L}/\text{min}$, the peak values of the higher-order harmonics (at $f^* > 1$), subharmonics and other components are continuously increasing, while accompanied with the decreasing numbers of peaks, as can be observed from Figure 10(c-d). This indicates a reduced nonlinearity with Q and Z_l , as have been shown in Figure 7.

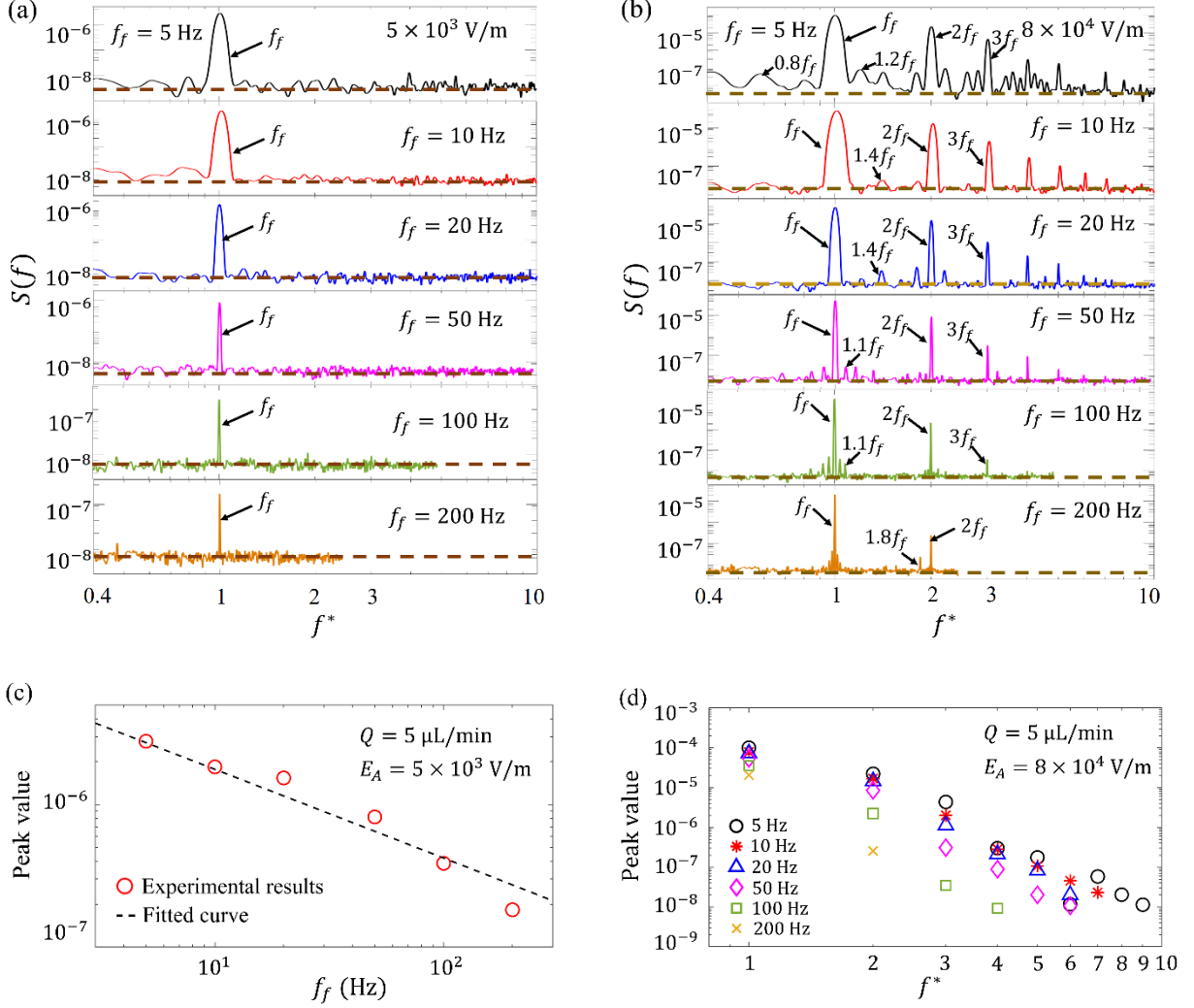


Figure 11 (a-b) Power spectrum of u' under different f_f at $Q = 5$ $\mu\text{L}/\text{min}$. The sampling rate is 1 kHz. Here, $\sigma = 6.08$ $\mu\text{S}/\text{cm}$ and $\text{pH} = 7.11$. The dashed lines indicate the noise level of unforced flow. (a) $E_A = 5 \times 10^3$ V/m, (b) $E_A = 8 \times 10^4$ V/m. (c-d) Peak values of $S(f)$ at different E_A . (c) $E_A = 2 \times 10^4$ V/m, (d) $E_A = 8 \times 10^4$ V/m.

3) $S(f)$ of u' varies with f_f

From the investigations in section 4.2, it has been shown the nonlinearity is decreased with f_f . This trend is further validated by the $S(f)$ of u' in Figure 11. When $E_A = 5 \times 10^3$ V/m, the electric field is not sufficiently high to generate nonlinear AC EOF for $f_f \in [5, 200]$ Hz. There is only a single peak at $f^* = 1$ for all f_f , as shown in Figure 11(a). Increasing f_f only leads to a fast decrease of the peak value at $f^* = 1$, approximately following a power-law curve as $f_f^{-0.62}$ (Figure 11(c)). The scaling exponent -0.62 is closely coincident with the -0.66

observed by Zhao et al. (2018) in linear AC EOF. When $E_A = 8 \times 10^4$ V/m (Figure 11(b)), as f_f is increased from 5 to 200 Hz, the rich peaks observed at the harmonics, subharmonics, and other components of $S(f)$ gradually disappear (Figure 11(d)), indicating a reduced nonlinearity with increasing f_f .

4.4 Critical dimensionless parameters for different chemical conditions

Generally say, the variations of AC EOF along E_A , f_f and Q based on statistics, time series, and spectrum all exhibit the same trends. These results are also consistent with the experimental investigations of Hu et al. (2022). However, all the experiments were conducted at $\sigma = 6.08$ $\mu\text{S}/\text{cm}$ and $\text{pH} = 7.11$. In this section, the influence of pH values and electric conductivities on the transitional electric field are investigated, through $Z_l \sim Z_{nlc}$ plots in a wide parameter space (by changing chemical conditions), where $Z_{nlc} = E_{A,C} z^2 \mu D_i / 2 |\zeta| \lambda^2 \rho_f f_f^2 l_0$ is the Z_{nl} calculated by $E_{A,C}$. In experiments, the conductivity and pH value of the solution is adjusted by adding 1X phosphate buffered saline (PBS) solution.

The experimental results are plotted with red dots in Figure 12. It can be seen that when $\text{pH} = 7.11$ (Figure 12(a)), Z_{nlc} gradually increases with the increase of Z_l . When $Z_{nl} \geq Z_{nlc}$, the AC EOF turns into a nonlinear regime, otherwise, the AC EOF is in a linear regime. When $\text{pH} = 7.36$ (Figure 12(b)), in the same range of Z_l , Z_{nlc} increases

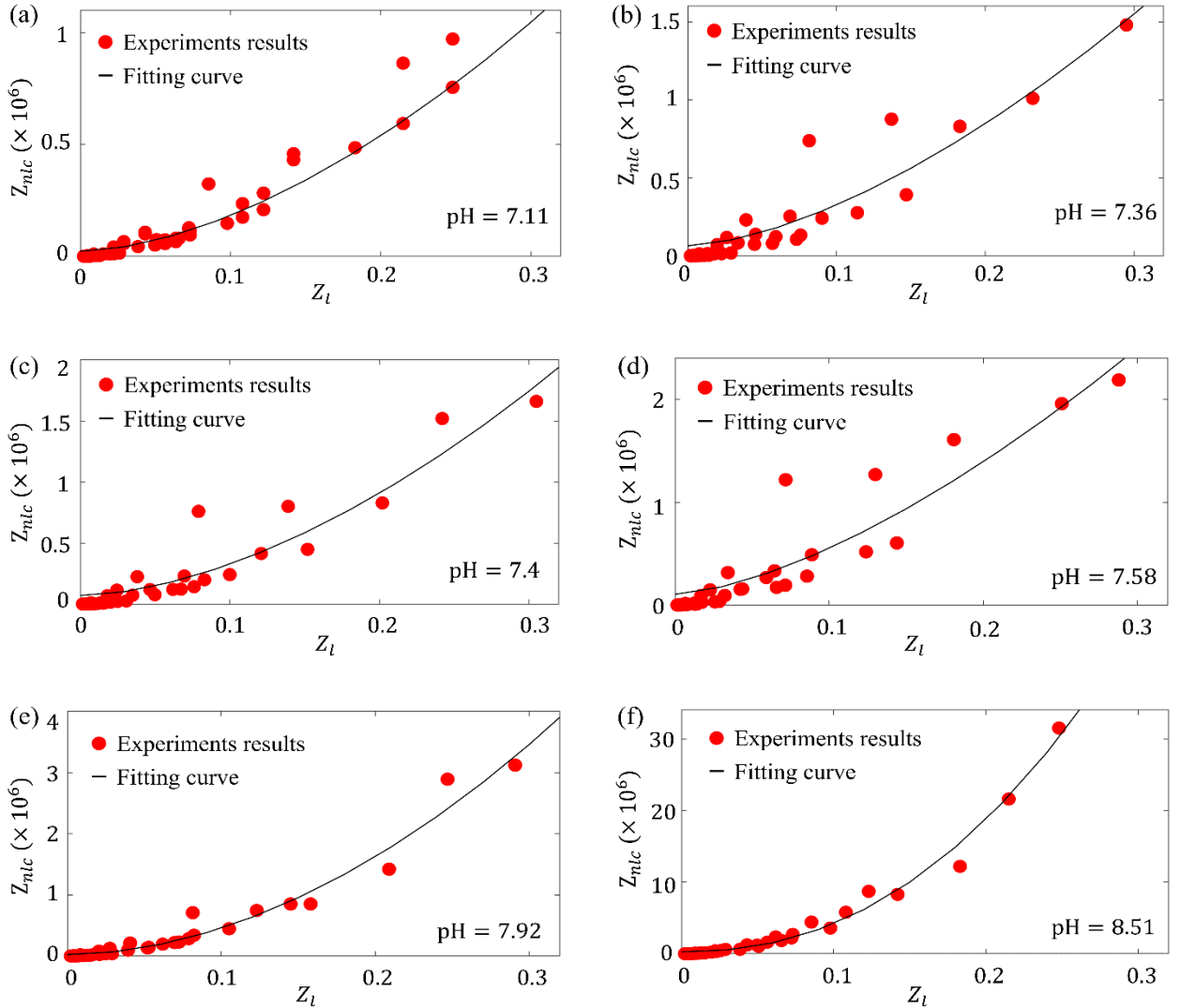


Figure 12 Relationship between Z_l and Z_{nlc} in six solutions with different pH values. (a) Fluorescent solution without PBS, $\sigma = 6.08 \mu\text{S/cm}$, $\text{pH}=7.11$; (b) fluorescent solution with PBS, $\sigma = 10.43 \mu\text{S/cm}$, $\text{pH}=7.36$; (c) fluorescent solution with PBS, $\sigma = 14.89 \mu\text{S/cm}$, $\text{pH}=7.4$; (d) fluorescent solution with PBS, $\sigma = 25.6 \mu\text{S/cm}$, $\text{pH}=7.58$; (e) fluorescent solution with PBS, $\sigma = 41.6 \mu\text{S/cm}$, $\text{pH}=7.92$; (f) fluorescent solution with PBS, $\sigma = 86 \mu\text{S/cm}$, $\text{pH}=8.51$.

with Z_l at a little faster rate than that of $\text{pH} = 7.11$. At $Z_l = 0.3$, the Z_{nlc} is around 1.5×10^6 at $\text{pH} = 7.36$, while that at $\text{pH} = 7.11$ is only 1×10^6 . As the pH value is further increased from 7.4 to 8.51 (Figure 12(c-f)), Z_{nlc} increases at a significantly larger increasing rate. The larger the pH value, the higher the Z_{nlc} is required, which in turn requires a higher critical electric field $E_{A,C}$. Or in other words, it is more difficult for the AC EOF to reach transition.

From Figure 12, even though all the data points show some scattering, they can perfectly fall on nonlinear curves expressed by a power-law relationship as below

$$Z_{nlc} = aZ_l^b + c \quad (16)$$

The fitting results are plotted in Figure 12 with black curves. The experimental results and the fitting curve are highly consistent. Below the $Z_l \sim Z_{nlc}$ curve, the linear behavior of the AC EOF is dominant. While above the $Z_l \sim Z_{nlc}$ curve, the nonlinear behavior of the AC EOF becomes non-negligible.

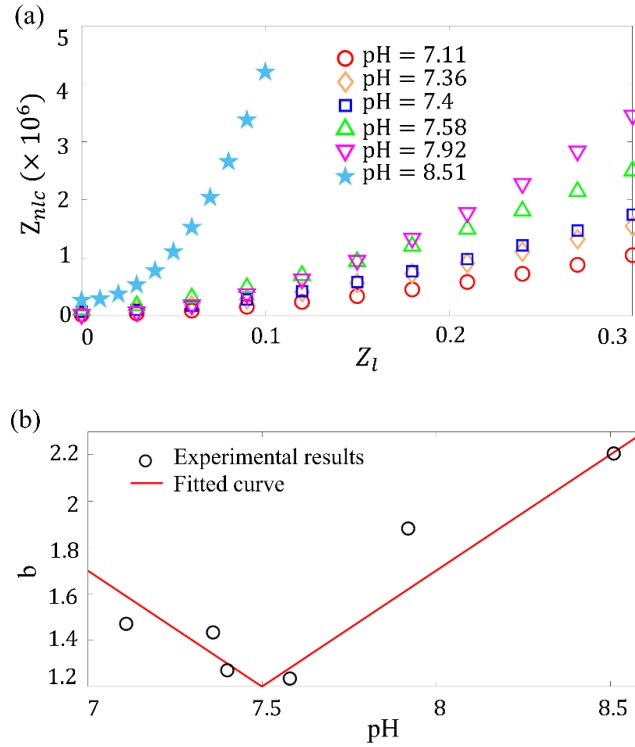


Figure 13 (a) Numerically fitted $Z_l \sim Z_{nlc}$ curves under different pH values. (b) Relationship between the scaling exponent b and pH value.

For a direct comparison, all six fitting curves are plotted in Figure 13(a). It can be found that the bending of $Z_l \sim Z_{nlc}$ curves changes with the pH. The bending of $Z_l \sim Z_{nlc}$ curve can be directly reflected by the scaling index b which is related to the pH value according to

$$\ln q_1 + \ln|\zeta|^{-1} + \ln(1 - q_2|\zeta|) = b \ln Z_l \quad (17)$$

where $q_1 = \frac{Z_{nlc}|\zeta|}{a}$ and $q_2 = \frac{c}{Z_{nlc}|\zeta|}$. Since $|\zeta| \sim O(10 \text{ mV})$ and $c/Z_{nlc} < 1$, $|\zeta|$ and $q_2|\zeta|$ are both below unity.

By Taylor expansion with only the first-order term reserved, Eq. (17) can be approximated as

$$b(\text{pH}) \approx \frac{\ln q_1 - 1}{\ln Z_l} - \frac{1 + q_2}{\ln Z_l} |\zeta| \quad (18)$$

Furthermore, Behrens and Grier (2001) theoretically show that $\zeta \sim \text{pH} - \text{pK}$ where pK is the dissociation constant, Eq. (18) can be established with a form of $b(\text{pH}) = b_0 + b_1|\text{pH} - \text{pK}|$. Based on Figure 13(b), it can be seen that the relationship between b and pH can be approximately fitted by

$$b = 1.2 + |\text{pH} - \text{pK}| \quad (19)$$

Here, $\text{pK} = 7.5$ (Xue *et al.* 2018). The nonlinear fitting is consistent with the theoretical analysis above.

4.5 Evaluation of the error of the model

To evaluate the possible deviations caused by the nonlinear fitting results of Eqs. (16) and (19), we define a deviation function:

$$\text{err}(Z_l) = \log \frac{Z_{nlc} - c}{aZ_l^{(1.2+|\text{pH}-\text{pK}|)}} \quad (20)$$

The function $\text{err}(Z_l)$ describes the relative derivation between the fitting results of Eqs. (16) and (19) and the experimental results. If Eqs. (16) and (19) can comprehensively and accurately describe the $Z_l \sim Z_{nlc}$ relationship, $\text{err}(Z_l)$ is close to zero. Here, we take all the six data groups with different pH values into account. The result is diagramed in Figure 14. It can be found that $\text{err}(Z_l)$ are primarily located around 0, which supports the effectiveness of Eqs. (16) and (19) for comprehensively describing the relationship between $Z_l \sim Z_{nlc}$. With the increase of Z_l , $\text{err}(Z_l)$ distribution narrows down to aggregate around 0, showing that Eqs. (16) and (19) can describe the $Z_l \sim Z_{nlc}$ relationship with much better accuracy at larger Z_l . All in all, the error analysis supports the effectiveness of Eqs. (16) and (19) to describe the $Z_l \sim Z_{nlc}$ relationship in a wide range of pH values.

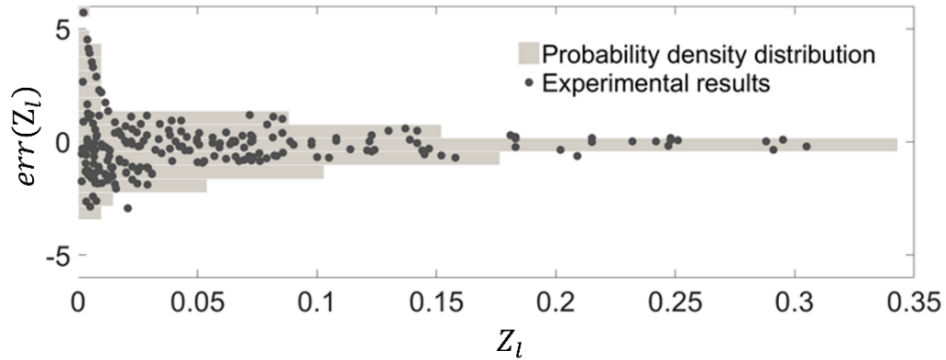


Figure 14 Under all the six pH values, the relative error between the fitting curve relying on Eqs. (16) and (19) and the experimental results.

5. Conclusion

In this investigation, AC EOF is theoretically and experimentally studied from the aspect of flow velocity in a broad parameter space, e.g. mean flow velocity, the frequency and intensity of the AC electric field, and the pH value of the bulk fluid. An electro-inertial velocity rather than the commonly applied Helmholtz-Smoluchowski velocity has been used as the characteristic velocity, to show a comprehensive evaluation of these control parameters. After 1D simplification, the control equations of the AC EOF on the velocity field and the internal electric field can both

be described by 1D inviscid Burgers equation with an external driving term. The linear term coefficient Z_l and the nonlinear term coefficient Z_{nl} of the inviscid Burgers equation determine the status of the AC EOF.

A larger Z_l indicates the contribution of the linear term in the inviscid Burgers equation becomes increasingly important. The AC EOF exhibits a linear response to the external electric field. This could be realized by increasing the flow rate of basic flow and AC frequency. The peak value of the velocity spectrum at AC frequency shows a power-law relationship with the AC frequency as $f_f^{-0.62}$. In contrast, a larger Z_{nl} indicates the contribution of nonlinear term in the inviscid Burgers equation becomes increasingly important, probably attributed to a larger electric field or smaller AC frequency. The AC EOF exhibits a nonlinear response to the external electric field in many aspects, e.g. (1) an asymmetric time series of velocity fluctuations, (2) a nonlinear increase of u_{rms} with electric field intensity, and (3) the emergence of spectral peaks at higher-order harmonic frequencies of the AC frequency. Besides, RC dynamics play an important role in the evolution of nonlinear AC EOF.

The transitional electric field $E_{A,C}$ and the corresponding Z_{nlc} between the linear and nonlinear AC EOF is studied through experiments under different pH values. It is found that Z_{nlc} exhibits a power-law relationship with Z_l in the considered range, as $Z_{nlc} \sim Z_l^b$. The scaling exponent b is a function of pH value, as $b = 1.2 + |\text{pH} - \text{pK}|$. Therefore, when the solution has a pH value far from the dissociation value pK, a large b can be concluded. Z_{nlc} exhibits a rapid and strongly nonlinear increase with Z_l . This means, under a certain Z_l , a larger Z_{nlc} is normally required for a larger b at a larger $|\text{pH} - \text{pK}|$. It is more difficult for the AC EOF to be nonlinear at a larger $|\text{pH} - \text{pK}|$.

From this research, we hope to fill the blank of experimental research in the field of nonlinear AC EOF, to reveal the complex interaction between the dynamics of AC EOF and basic flow. In the meanwhile, the investigation could have important guiding significance for the practical application in micro-/nanofluidics, electric energy systems and devices, electrochemistry, and other fields. By properly selecting the control parameters, e.g. Z_l and Z_{nl} , people can effectively generate or suppress nonlinear EOF and accurately control the flow status of the fluid, so as to achieve either enhancement of heat and mass transfer, or reducing electrical energy loss and improving energy efficiency.

6. References

- AGAR, E., KNEHR, K.W., CHEN, D., HICKNER, M.A. & KUMBUR, E.C. 2013 Species transport mechanisms governing capacity loss in vanadium flow batteries: Comparing Nafion and sulfonated Radel membranes. *Electrochim. Acta* **98** (30), 66-74.
- ARIMA, A., TSUTSUI, M., WASHIO, T., BABA, Y. & KAWAI, T. 2021 Solid-State Nanopore Platform Integrated with Machine Learning for Digital Diagnosis of Virus Infection. *Anal. Chem.* **93** (1), 215-227.
- BAZANT, M.Z. & SQUIRES, T.M. 2004 Induced-charge electro-osmosis. *J. Fluid Mech.* **509** (25), 217-252.
- BAZANT, M.Z., THORNTON, K. & AJDARI, A. 2004 Diffuse-Charge Dynamics in Electrochemical Systems. *Phys. Rev. E* **70** (2), 021506.
- BEHRENS, S.H. & GRIER, D.G. 2001 The charge of glass and silica surfaces. *J. Chem. Phys.* **115** (14), 6716-6721.
- BERA, S. & BHATTACHARYYA, S. 2013 On mixed electroosmotic-pressure driven flow and mass transport in microchannels. *Int. J. Eng. Sci.* **62**, 165-176.
- BHATTACHARYYA, S. & GOPMANDAL, P.P. 2013 Effects of electroosmosis and counterion penetration on electrophoresis of a positively charged spherical permeable particle. *Soft Matter* **9** (6), 1871.
- BOWN, M.R. & MEINHART, C.D. 2006 AC electroosmotic flow in a DNA concentrator. *Microfluid. Nanofluid.* **2** (6), 513-523.
- CHAKRABORTY, S. & SRIVASTAVA, A.K. 2007 Generalized model for time periodic electroosmotic flows with overlapping electrical double layers. *Langmuir* **23** (24), 12421.

- DAS, S. & CHAKRABORTY, S. 2007 Transverse electrodes for improved DNA hybridization in microchannels. *AIChE J.* **53** (5), 1086-1099.
- DAS, S., SUBRAMANIAN, K. & CHAKRABORTY, S. 2007 Analytical investigations on the effects of substrate kinetics on macromolecular transport and hybridization through microfluidic channels. *Colloids Surf., B* **58** (2), 203-217.
- DUTTA, P. & BESKOK, A. 2001 Analytical solution of time periodic electroosmotic flows: analogies to Stokes' second problem. *Anal. Chem.* **73** (21), 5097-5102.
- FENG, G. & CUMMINGS, P.T. 2011 Supercapacitor Capacitance Exhibits Oscillatory Behavior as a Function of Nanopore Size. *J. Phys. Chem. Lett.* **2** (22), 2859-2864.
- GAGNON, Z. & CHANG, H.-C. 2005 Aligning fast alternating current electroosmotic flow fields and characteristic frequencies with dielectrophoretic traps to achieve rapid bacteria detection. *Electrophoresis* **26** (19), 3725-3737.
- HAN, J.-H., MURALIDHAR, R., WASER, R. & BAZANT, M.Z. 2016 Resistive Switching in Aqueous Nanopores by Shock Electrodeposition. *Electrochim. Acta* **222** (20), 370-375.
- HOJGAARD OLESEN, L., BAZANT, M.Z. & BRUUS, H. 2010 Strongly nonlinear dynamics of electrolytes in large ac voltages. *Phys. Rev. E* **82** (1), 011501.
- HU, Z., ZHAO, T., WANG, H., ZHAO, W., WANG, K., BAI, J. & WANG, G. 2020 Asymmetric temporal variation of oscillating AC electroosmosis with a steady pressure-driven flow. *Exp. Fluids* **61** (11), 233.
- HU, Z., ZHAO, T., ZHAO, W., YANG, F., WANG, H., WANG, K., BAI, J. & WANG, G. 2021 Transition from periodic to chaotic AC electroosmotic flows near electric double layer. *AIChE J.* **67** (4), e17148.
- HU, Z., ZHAO, W., CHEN, Y., HAN, Y., ZHANG, C., FENG, X., JING, G., WANG, K., BAI, J., WANG, G. & ZHAO, W. 2022 Onset of Nonlinear Electroosmotic Flow under an AC Electric Field. *Anal. Chem.* **94** (51), 17913-17921.
- JI, J., LI, P., SANG, S., ZHANG, W., ZHOU, Z., YANG, X., DONG, H., LI, G. & HU, J. 2014 Electrodeposition of Au/Ag bimetallic dendrites assisted by Faradaic AC-electroosmosis flow. *AIP Adv.* **4** (3), 031329.
- JIAN, Y.J., LIU, Q.S. & YANG, L.G. 2011 AC electroosmotic flow of generalized Maxwell fluids in a rectangular microchannel. *J. Non-Newtonian Fluid Mech.* **166** (21), 1304-1314.
- KHODABANDEHLOO, A. & CHEN, D.D.Y. 2017 Electroosmotic Flow Dispersion of Large Molecules in Electrokinetic Migration. *Anal. Chem.* **89** (15), 7823-7827.
- KNELLER, A.R., HAYWOOD, D.G. & JACOBSON, S.C. 2016 AC Electroosmotic Pumping in Nanofluidic Funnel. *Anal. Chem.* **88** (12), 6390-6394.
- LEI, K.F., CHENG, H., CHOY, K.Y. & CHOW, L.M.C. 2009 Electrokinetic DNA concentration in microsystems. *Sens. Actuators, A* **156** (2), 381-387.
- LEONG, I.W., TSUTSUI, M., MURAYAMA, S., HE, Y. & TANIGUCHI, M. 2020 Electroosmosis-Driven Nanofluidic Diodes. *J. Phys. Chem. B* **124** (32), 7086-7092.
- LIU, W., REN, Y., XUE, R., SONG, C. & WU, Q. 2020 On ion transport regulation with field-effect nonlinear electroosmosis control in microfluidics embedding an ion-selective medium. *Electrophoresis* **41** (10-11), 778-792.
- MARTIN, L., ALIZADEH, V. & MEEGODA, J. 2019 Electro-osmosis treatment techniques and their effect on dewatering of soils, sediments, and sludge: A review. *Soils Found.* **59** (2), 407-418.
- PARK, H.M. & LEE, W.M. 2008 Helmholtz–Smoluchowski velocity for viscoelastic electroosmotic flows. *J. Colloid Interface Sci.* **317** (2), 631-636.
- PROBSTEIN, R.F. & HICKS, R.E. 1993 Removal of Contaminants from Soils by Electric Fields. *Science* **260** (5107), 498-503.
- RAMOS, A., MORGAN, H., GREEN, N.G., GONZÁLEZ, A. & CASTELLANOS, A. 2005 Pumping of liquids with traveling-wave electroosmosis. *J. Appl. Phys.* **97** (8), 084906.
- ROMANYUK, K., COSTA, C.M., LUCHKIN, S.Y., KHOLKIN, A.L. & LANCEROS-MENDEZ, S. 2016 Giant electric field-induced strain in PVDF-based battery separator membranes probed by Electrochemical Strain Microscopy. *Langmuir* **32**

- (21), 5267-5276.
- RUBIN, S., TULCHINSKY, A., GAT, A.D. & BERCOVICI, M. 2016 Elastic deformations driven by non-uniform lubrication flows. *J. Fluid Mech.* **812**, 841-865.
- RUBINSTEIN, I. & ZALTZMAN, B. 2000 Electro-osmotically induced convection at a permselective membrane. *Phys. Rev. E* **62** (2), 2238-2251.
- RUBINSTEIN, S.M., MANUKYAN, G., STAIKU, A., RUBINSTEIN, I., ZALTZMAN, B., LAMMERTINK, R.G., MUGELE, F. & WESSLING, M. 2008 Direct observation of a nonequilibrium electro-osmotic instability. *Phys. Rev. Lett.* **101** (23), 236101.
- SANTIAGO, J.G., WERELEY, S.T., MEINHART, C.D., BEEBE, D.J. & ADRIAN, R.J. 1998 A particle image velocimetry system for microfluidics. *Exp. Fluids* **25** (4), 316-319.
- SCHNITZER, O. & YARIV, E. 2014 Nonlinear oscillations in an electrolyte solution under ac voltage. *Phys. Rev. E* **89** (3), 032302.
- SHI, Y., ZENG, M., BAI, H., MENG, S., ZHANG, C., FENG, X., ZHANG, C., WANG, K. & ZHAO, W. 2023 Transition Routes of Electrokinetic Flow in a Divergent Microchannel with Bending Walls. *Micromachines* **14** (2), 474.
- SPHAIER, L.A. 2012 Integral transform solution for heat transfer in parallel-plates micro-channels: Combined electroosmotic and pressure driven flows with isothermal walls. *Int. Commun. Heat Mass Transfer* **39** (6), 769-775.
- STOUT, R.F. & KHAIR, A.S. 2015 Moderately nonlinear diffuse-charge dynamics under an ac voltage. *Phys. Rev. E* **92** (3), 032305.
- SUH, Y.K. & KANG, S. 2008 Asymptotic analysis of ion transport in a nonlinear regime around polarized electrodes under ac. *Phys. Rev. E* **77** (3), 031504.
- SUH, Y.K. & KANG, S. 2009 Numerical prediction of ac electro-osmotic flows around polarized electrodes. *Phys. Rev. E* **79** (4), 046309.
- WANG, B., GUO, W. & FU, Y. 2020 Anodized Aluminum Oxide Separators with Aligned Channels for High-Performance Li-S Batteries. *ACS Appl. Mater. Interfaces* **12** (5), 5831-5837.
- WANG, G., YANG, F., ZHAO, W. & CHEN, C.P. 2016 On micro-electrokinetic scalar turbulence in microfluidics at a low Reynolds number. *Lab Chip* **16** (6), 1030-1038.
- WANG, G.R. 2005 Laser induced fluorescence photobleaching anemometer for microfluidic devices. *Lab Chip* **5** (4), 450-456.
- WANG, G.R., YANG, F. & ZHAO, W. 2014 There can be turbulence in microfluidics at low Reynolds number. *Lab Chip* **14** (8), 1452-1458.
- WANG, X.Y., CHENG, C., WANG, S.L. & LIU, S.R. 2009 Electroosmotic pumps and their applications in microfluidic systems. *Microfluid. Nanofluid.* **6** (2), 145-162.
- WONG, P.K., CHEN, C.P., WANG, G. & HO, C.M. 2004 Electrokinetic bioprocessor for concentrating cells and molecules. *Anal. Chem.* **76** (23), 6908-6914.
- WU, C., HUANG, W. & HU, C. 2015 An ultrasensitive label-free electrochemical impedimetric DNA biosensing chip integrated with a DC-biased AC electroosmotic vortex. *Sens. Actuators, B* **209**, 61-68.
- WU, M., GAO, Y., GHAZNAVI, A., ZHAO, W. & XU, J. 2022 AC electroosmosis micromixing on a lab-on-a-foil electric microfluidic device. *Sens. Actuators, B* **359** (15), 131611.
- WU, W.-I., EWING, D., CHING, C.Y. & SELVAGANAPATHY, P.R. 2013 Measurement of periodic micro flows using micro-particle image velocimetry with phase sampling. *Microfluid. Nanofluid.* **15** (1), 127-135.
- WU, Z. & CHEN, X. 2019 Numerical simulation of a novel microfluidic electroosmotic micromixer with Cantor fractal structure. *Microsyst. Technol.* **25**, 3157-3164.
- XUE, J., ZHAO, W., NIE, T., ZHANG, C., MA, S., WANG, G., LIU, S., LI, J., GU, C., BAI, J. & WANG, K. 2018 Abnormal Rheological Phenomena in Newtonian Fluids in Electroosmotic Flows in a Nanocapillary. *Langmuir* **34** (50), 15203-

15210.

- YANG, F., YANG, X., JIANG, H., BULKHAULTS, P., WOOD, P., HRUSHESKY, W. & WANG, G. 2010 Dielectrophoretic separation of colorectal cancer cells. *Biomicrofluidics* **4** (1), 13204.
- YANG, X.G., YE, Q., CHENG, P. & ZHAO, T.S. 2015 Effects of the electric field on ion crossover in vanadium redox flow batteries. *Appl. Energy* **145** (1), 306-319.
- YOSSIFON, G. & CHANG, H.C. 2008 Selection of nonequilibrium overlimiting currents: universal depletion layer formation dynamics and vortex instability. *Phys. Rev. Lett.* **101** (25), 254501.
- YU, Y., LI, J., LIN, H., LI, K. & YI, F. 2023 Study on ethanol driven by alternating current electroosmosis in microchannels. *Sens. Actuators, A* **351** (1), 114174.
- ZALTZMAN, B. & RUBINSTEIN, I. 2007 Electro-osmotic slip and electroconvective instability. *J. Fluid Mech.* **579** (25), 173-226.
- ZHAO, C. & YANG, C. 2013 Electroosmotic flows of non-Newtonian power-law fluids in a cylindrical microchannel. *Electrophoresis* **34** (5), 662-667.
- ZHAO, W., LIU, X., YANG, F., WANG, K., BAI, J., QIAO, R. & WANG, G. 2018 Study of Oscillating Electroosmotic Flows with High Temporal and Spatial Resolution. *Anal. Chem.* **90** (3), 1652-1659.
- ZHAO, W., SU, W. & WANG, G. 2021 Interactions of velocity structures between large and small scales in microelectrokinetic turbulence. *Phys. Rev. Fluids* **6** (7), 074610.
- ZHAO, W., YANG, F., KHAN, J., REIFSNIDER, K. & WANG, G. 2016 Measurement of velocity fluctuations in microfluidics with simultaneously ultrahigh spatial and temporal resolution. *Exp. Fluids* **57** (11), 1-12.
- ZHAO, W., YANG, F., WANG, K., BAI, J. & WANG, G. 2017 Rapid mixing by turbulent-like electrokinetic microflow. *Chem. Eng. Sci.* **165**, 113-121.